Time-Optimal Transfers Between Planar Solar-Sail Libration Point Orbits

R.J. de Boer

Delft University of Technology

TUDelft Delft University of Technology

Challenge the future

Time-Optimal Transfers Between Planar Solar-Sail Libration Point Orbits

R.J. de Boer

1146068

A thesis submitted to the Faculty of Aerospace Engineering
of the Delft University of Technology
in partial fulfillment of the requirements for the degree of
Master of Science in Aerospace Engineering

April 1, 2020

Thesis Committee:	Prof. P.N.A.M. Visser	Chair
	Dr. M.J. Heiligers	Daily Supervisor
	Dr. J. Guo	External Examiner

Cover image credit : Techpoke, http://www.techpoke.com/wp-content/uploads/2015/03/solar-sail.jpg

Delft
University of
Technology

Executive Summary

Using solar radiation pressure to propel a spacecraft is a concept that dates back to the early rocket pioneers at the beginning of the 20th century. A solar sail provides propulsion by momentum exchange with incoming photons of light, instead of by expelling reaction mass, as most spacecraft do. Because it is not possible to refuel in space, the propulsive capabilities of current space missions are limited by their stock of propellant. In contrast, solar sails are capable of providing thrust indefinitely, which allows them to potentially reach velocities unattainable by conventional spacecraft. Furthermore, augmenting the gravitational acceleration with constant propulsive acceleration allows for non-Keplerian trajectories to be flown, which opens up new possibilities for mission design.

There has been renewed interest in solar sails in recent years. Small demonstrator missions have been flown in Earth orbit, showing that it is possible to deploy large, thin membranes in space, and that they can be used to raise the orbit altitude. Recent work has found novel solar-sail displaced libration point orbits in the Sun-Earth and Earth-Moon systems. These orbits are useful for a number of applications, including observation and communication capabilities for the polar regions of the Earth and Moon, space weather monitoring, astronomical observation, and space physics research. Because solar sails possess essentially unlimited propulsive endurance, they provide the possibility of increasing the scientific value of a single spacecraft by visiting multiple different orbits over the course of a mission. Transfers trajectories between these orbits may therefore be of use to future mission design, and have not been investigated before.

This report presents time-optimal transfer trajectories between solar-sail displaced orbits around the L_1 and L_2 points of the Sun-Earth and Earth-Moon systems. Such trajectories may be useful for designing future missions that investigate the space environment in the vicinity of the Earth and Moon. Furthermore, the methods described in this paper can be extended to find trajectories between a wider range of solar-sail displaced orbits.

Initial guess trajectories are generated as two-segment transfers, where the sail attitude along each segment is fixed. The discontinuity between the two segments is minimized by means of a genetic-algorithm approach. These trajectories are then optimized by two methods: multiple shooting with differential correction, and pseudo-spectral collocation. The results of these two methods are compared.

In the Sun-Earth system, both methods yield good results, with transfer times as short as 91 days for transfers between L_1 and L_2 orbits, and transfer times as short as 29 days for transfers between orbits around the same libration point. Pseudo-spectral collocation generally yielded slightly faster trajectories, with a smoother and more continuous control profile.

In the Earth-Moon system, pseudospectral collocation failed to yield practically feasible trajectories, proving unable to handle the time-dependency introduced into the dynamics by the apparent rotation of the Sun around the system. The differential corrector found trajectories with transfer times as short as 15.6 days, but the associated control profiles feature large discontinuous jumps in the cone angle of the sail, which are likely to be problematic in practice.

Contents

List of Symbols

Latin Symbols

A	Matrix of state vector partial derivatives	(-)
C	Matrix of partial derivatives of constraints w.r.t. state variables	(-)
G	Endpoint cost function	(-)
J	Cost function	(-)
J_{GA}	Genetic algorithm cost function	(-)
L	Integral cost function	(-)
M	Matrix of partial derivatives of $\Delta\mathbf{V}$ w.r.t. state variables	(-)
P_{arr}	Period of the arrival orbit	(-)
P_{dep}	Period of the departure orbit	(-)
P_{max}	Largest period of either the departure or arrival orbit	(-)
$\hat{\mathbf{S}}$	Sun-line vector	(-)
$\hat{\mathbf{S}}_{EM}$	Sun-line vector in the Earth-Moon system	(-)
TF	Flight time	(-)
TF_{arr}	Flight time of arrival trajectory segment	(-)
TF_{dep}	Flight time of departure trajectory segment	(-)
T^{*}_{arr}	Time along the arrival orbit	(-)
T^{*}_{con}	Time of arrival - departure segment connection	(-)
T^{*}_{dep}	Time along the departure orbit	(-)
T^{*}	Flight time of converged orbit	(-)
U	Gravitational potential	(-)
$\mathbf{V}$	Velocity vector	(-)
$\mathbf{V}_i^-$	Incoming velocity vector at node i	(-)
$\mathbf{V}_i^+$	Outgoing velocity vector at node i	(-)
$\mathbf{X}$	State vector	(-)
$\mathbf{X}_a$	Fourier approximation of arrival orbit state vector	(-)
$\mathbf{X}_d$	Fourier approximation of departure orbit state vector	(-)
$\mathbf{X}_i$	State vector at node i	(-)
$a_{0,EM}$	Characteristic sail acceleration	(-)
$\mathbf{a}_s$	Solar-sail acceleration vector	(-)

$\mathbf{a}_{S,SE}$	Solar-sail acceleration vector in the Sun-Earth system	(-)
$a_{s,x}$	Component of solar-sail acceleration along the x-axis	(-)
$a_{s,y}$	Component of solar-sail acceleration along the y-axis	(-)
$a_{s,z}$	Component of solar-sail acceleration along the z-axis	(-)
$\mathbf{c}$	Vector of constraint values	(-)
$c_{i,k}$	Constraint k acting on node i	(-)
$\mathbf{g}_{EM}$	Genetic algorithm decision vector in the Earth-Moon system	(-)
$\mathbf{g}_{SE}$	Genetic algorithm decision vector in the Sun-Earth system	(-)
i	Node number	(-)
j	Node number	(-)
k	Constraint number	(-)
m_1	Mass of the larger primary body	(kg)
m_2	Mass of the smaller primary body	(kg)
$\hat{\mathbf{n}}$	Solar-sail normal vector	(-)
n	Total number of nodes	(-)
$\mathbf{p}$	Vector of static optimization parameters	(-)
r	Position	(-)
$\mathbf{R}$	Position vector	(-)
$\mathbf{r}$	Position vector	(-)
r_1	Distance to larger primary body	(-)
r_2	Distance to smaller primary body	(-)
t	Time	(-)
t_0	Start time	(-)
t_f	End time	(-)
$\mathbf{u}$	Control vector	(-)
v	Velocity	(-)
w_v	Velocity deviation weight factor	(-)
$\mathbf{x}$	State vector	(-)
x	Position along the x-axis	(-)
$\mathbf{x}_0$	Start state vector	(-)
$\mathbf{x}_f$	End state vector	(-)
y	Position along the y-axis	( )
	Greek Symbols	
$\Delta\mathbf{V}$	Vector of velocity discontinuities at the nodes	(-)

Φ	State transition matrix	(-)
Φ_{RR}	State transition submatrix of position w.r.t. position	(-)
Φ_{RV}	State transition submatrix of position w.r.t. velocity	(-)
$\Phi_{R\alpha}$	State transition submatrix of position w.r.t. cone angle	(-)
Φ_{VR}	State transition submatrix of velocity w.r.t. position	(-)
Φ_{VV}	State transition submatrix of velocity w.r.t. velocity	(-)
$\Phi_{V\alpha}$	State transition submatrix of velocity w.r.t. cone angle	(-)
$\Phi_{\alpha R}$	State transition submatrix of cone angle w.r.t. position	(-)
$\Phi_{\alpha V}$	State transition submatrix of cone angle w.r.t. velocity	(-)
$\Phi_{\alpha\alpha}$	State transition submatrix of cone angle w.r.t. cone angle	(-)
Ω_S	Angular rate of the Sun around the Earth-Moon system	(-)
α	Solar-sail cone angle	(deg)
α_{arr}	Fixed cone angle of the arrival trajectory segment	(deg)
α_{dep}	Fixed cone angle of the departure trajectory segment	(deg)
β	Solar-sail lightness number	(-)
$\varphi_{i,j}$	Matrix of partial derivatives of state variables at node i to those at node j	(-)
μ	Mass of the smaller primary body as a fraction of total system mass	(-)
ω	Angular velocity of the CR3BP reference frame	(-)
$\boldsymbol{\omega}$	Angular velocity vector of the CR3BP reference frame	( )
$(\dot{\ })$	First-order derivative w.r.t. time	(-)
$(\ddot{\ })$	Second-order derivative w.r.t. time	(-)

Abbreviations

$CR3BP$	Circular Restricted Three-Body Problem
DC	Differential Corrector
$MSDC$	Multiple Shooting Differential Correction
LGL	Legendre-Gauss-Lobatto
NLP	Non-Linear Programming
STM	State Transition Matrix

Subscripts

EM	Property in the Earth-Moon system
SE	Property in the Sun-Earth system

List of Figures

List of Tables

1

Introduction

This chapter contains an introduction to the thesis work that is presented in this report. Section 1.1 provides a conceptual background by providing a short overview of the history and applications of solar sailing. Section 1.2 places the report in the context of prior work on transfers between solar-sail displaced libration point orbits. The research objective and associated research questions are presented in section 1.3. Finally, section 1.4 describes the structure of the remainder of this report.

1.1. Solar Sailing

Conventional spacecraft achieve propulsion by momentum exchange with some type of propellant, which is expelled from the spacecraft at high velocity. Because there is currently no means to refuel in space, all the propellant that will be needed throughout the course of a mission has to be brought from Earth when the spacecraft is launched. Because the propellant itself adds additional mass that must be accelerated, the amount of propellant that is needed increases exponentially with the required mission ΔV. This leads to a strict trade-off between propulsion and payload capabilities in mission design.

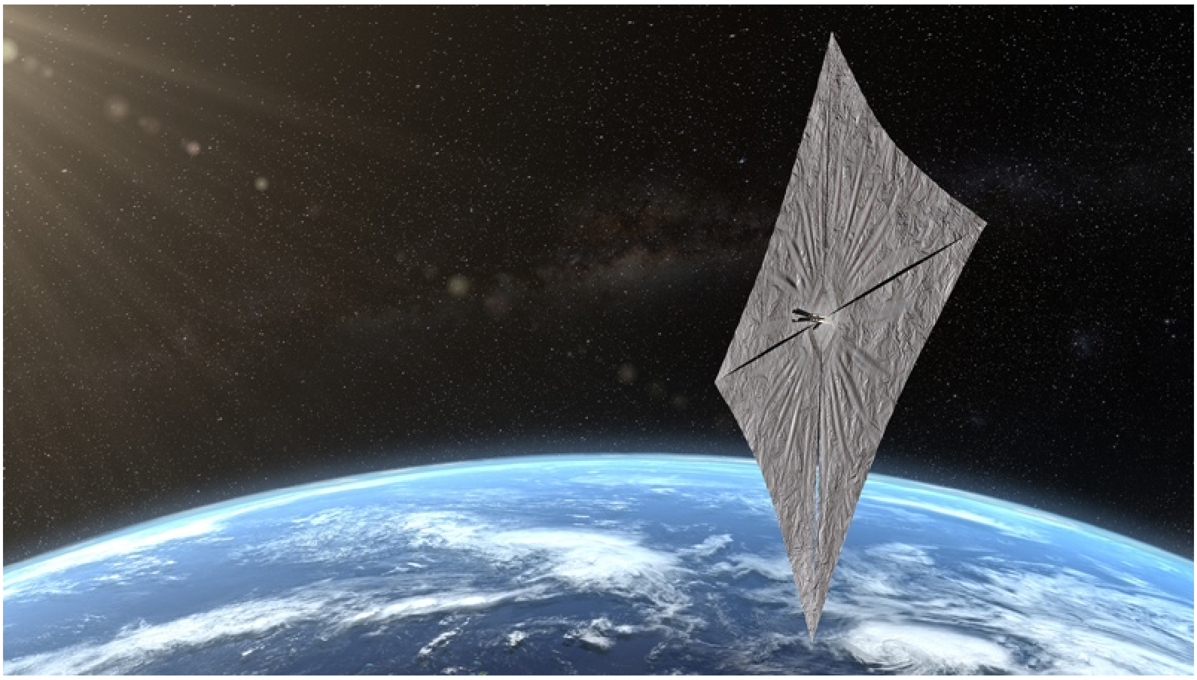

Figure 1.1: Artist conception of Lightsail-2 deployed in Earth orbit. Image credit: The Planetary Society.

Solar sails present an alternative to propellant-based propulsion techniques. A solar sail works by reflecting photons of incoming Sunlight off a large reflective sail. The photons hitting the sail are massless, but they do possess momentum. This momentum is exchanged with the sail twice: first when the sail temporarily absorbs the photon, and then again when the photon is re-emitted. In this way, the spacecraft is accelerated by making use of the energy in the ambient solar radiation pressure, analogous to the way a sailboat makes use of the terrestrial wind.

The potential of rocket propulsion through solar radiation pressure was recognized by early rocket pioneers like Tsander (1924), who envisioned a future where interplanetary vessels carried passengers through the solar system, propelled by enormous mirrors over a square kilometer in size collecting light beamed to them by even larger mirrors on orbiting stations. The term *solar sailing* was coined by Garwin (1958), who proposed using a thin, aluminium-coated plastic sail to propel a spacecraft to velocities that are unattainable by chemical propulsion. In subsequent years several papers explored the dynamics of solar-sail enabled interplanetary and Earth-escape trajectories (Tsu, 1959; Sands, 1961; Fimple, 1962), and NASA seriously considered using a solar sail for a rendezvous mission with Halley's Comet (Friedman et al., 1978). Concerns regarding the technological readiness of solar sails forestalled any actual mission however, and no solar sails were flown in this era (McInnes, 1999).

In recent years, there has been renewed interest in solar sailing. Through reductions in launch costs and standardized spacecraft platforms, small demonstrator missions have become relatively affordable, and the first solar sails have flown in space. The IKAROS mission has demonstrated propulsion and attitude control capabilities while en route to Venus (Sawada et al., 2011), NanoSail-D2 and Lightsail-1 were deployed in Earth orbit (Johnson et al., 2011; Betts et al., 2017), and Lightsail-2, displayed in Fig. 1.1, has successfully demonstrated Earth-bound orbit raising using solar-sail propulsion (Davis, 2019).

1.1.1. Solar-sail applications

The ability of solar sails to provide continuous acceleration without consuming propellant makes them suitable for a variety of mission applications. For interplanetary transfers, they are particularly competitive for high-energy trajectories, such as those required to fly to Mercury. For such transfers, the exponential nature of the rocket equation has required spacecraft with conventional propulsion to perform a number of gravity-assist maneuvers, which add complexity and lead to long flight times.

A unique application of solar sails is their ability to enable non-Keplerian orbits, by the addition of continuous thrust to the gravitational acceleration. These orbits can provide scientific observation and communication capabilities which can not otherwise be achieved. For example, near-future solar sails allow for displaced libration point orbits which can provide continuous coverage of the polar regions of the Earth (Ceriotti and McInnes, 2012) or Moon (Wawrzyniak and Howell, 2008), which is a capability that cannot be provided by conventional polar orbits. Other proposals include using a solar sail to access a displaced orbit Sunward of the Earth-Sun L_1 point to provide early warning of potentially damaging space weather events (West, 2004), and displacing geostationary orbits above or below the equatorial plane, greatly increasing the available orbital slots (McInnes, 1999).

Finally, solar sails could enable long duration missions visiting multiple locations, as there are no limits on their endurance, beyond eventual component failure. For example, a survey mission of near-Earth asteroids could visit many such objects, even if they are in widely separated orbits. Such long-duration capabilities would also be of use for missions that study the space environment, such as studies of the solar wind, or the magnetic fields of the Sun and planets, by providing measurements with increased spatial coverage.

1.2. Transfers between solar-sail libration point orbits

The focus of this thesis work is to find time-optimal transfer trajectories between solar-sail displaced libration point orbits in the Sun-Earth and Earth-Moon systems. Such transfers are of interest because they could greatly enhance the scientific value of a single spacecraft. For example, a spacecraft could transfer from a displaced orbit optimized for coverage of one of the poles of the Earth or Moon to one that is optimized to provide coverage of the other pole, or more fully measure the magnetic field of a planetary body by observations around both the Sunward and outer co-linear libration points.

To date, the only example of a transfer between libration point orbits was conducted during NASA's ARTEMIS mission (Sweetser et al., 2011). The objective of this mission was to investigate the effect of the Moon on the magnetic fields of the Earth and Sun by measuring the solar wind at various locations. Twin spacecraft were inserted into quasi-periodic Lissajous orbits around the L_1 and L_2 points of the Earth-Moon system. The trajectory of one of the two spacecraft, ARTEMIS-P1, is displayed in Fig.

1.2. After a period of initial observations in an L_2 orbit, ARTEMIS-P1 was transferred to an L_1 orbit. Conventional propulsion methods were used for both station-keeping and insertion into the libration point orbits (Folta et al., 2011). Similar future missions would benefit from solar-sail propulsion, which would allow an unlimited number of transfers between these orbits.

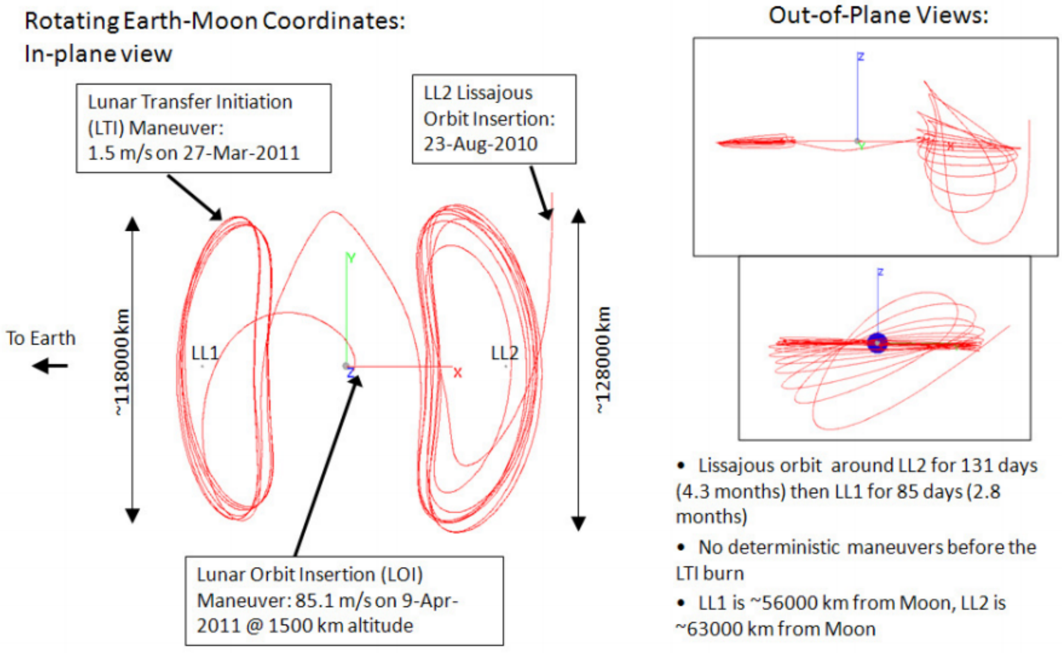
Rotating Earth-Moon Coordinates:
In-plane view

Lunar Transfer Initiation (LTI) Maneuver: 1.5 m/s on 27-Mar-2011

LL2 Lissajous Orbit Insertion: 23-Aug-2010

Lunar Orbit Insertion (LOI) Maneuver: 85.1 m/s on 9-Apr-2011 @ 1500 km altitude

Out-of-Plane Views:

- Lissajous orbit around LL2 for 131 days (4.3 months) then LL1 for 85 days (2.8 months)
- No deterministic maneuvers before the LTI burn
- LL1 is ~56000 km from Moon, LL2 is ~63000 km from Moon

Figure 1.2: Trajectory design for ARTEMIS-P1, including L_2 to L_1 transfer. Image credit: Sweetser et al. (2011)

The majority of the work on solar-sail trajectories has been concerned with finding interplanetary or Earth-escape trajectories. In comparison, transfers involving displaced libration point orbits have received less attention. Several studies have analyzed the use of solar-sail propulsion to reach the Sun-Earth triangular Lagrange points. Sood and Howell (2016) found transfer trajectories between a low Earth parking orbit and the L_5 point, Farres et al. (2019) investigated transfers from the L_1 and L_2 points to the region of practical stability of the L_4 and L_5 points, and Fernandez et al. (2018) found trajectories to the L_5 point, departing from solar-sail displaced orbits around the L_1 and L_2 points.

Recent work has found extended families of solar-sail displaced periodic orbits around the L_1 and L_2 points of the Earth-Moon system (Heiligers et al., 2016). For the planar Lyapunov orbits around these points, displayed in Fig. 1.3 for varying levels of sail performance, homoclinic and heteroclinic connections were found by Heiligers (2018). These connections depart and arrive along the unstable and stable manifolds of the orbits in question, and were not optimized for time of flight. Feasible trajectories between high Earth orbit and displaced vertical Lyapunov orbits around the Earth-Moon L_2 points were found by Van Den Oever and Heiligers (2018).

Time-optimal transfers between orbits around the co-linear L_1 and L_2 points have not yet been investigated in either the Sun-Earth or the Earth-Moon system.

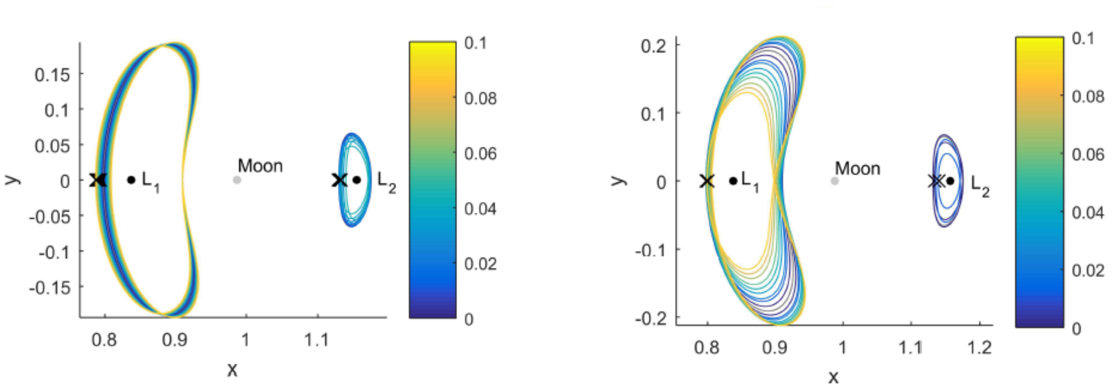

Figure 1.3: Displaced planar Lyapunov orbits around the Earth-Moon L_1 and L_2 points for different values of solar-sail acceleration under different sail steering laws. Image credit: Heiligers et al. (2016).

1.3. Research objective

The objective of this thesis is to add to the literature by finding time-optimal transfer trajectories between a number of solar-sail displaced libration point orbits around the L_1 and L_2 points of the Sun-Earth and Earth-Moon systems. Two methods for finding these trajectories will be compared: direct pseudospectral collocation and multiple shooting with differential correction. Such trajectories have not been studied before, and investigating the nature and control requirements of these trajectories will demonstrate the feasibility of using near-future solar-sail technology to improve the scientific output of future missions similar to ARTEMIS. Furthermore, the framework presented in this paper can be expanded to investigate transfers between a wider range of solar-sail orbits.

To achieve this objective, the following research questions have been formulated:

I *What are the time-optimal transfer trajectories between solar-sail displaced orbits around the colinear libration points of the the Sun-Earth and Earth-Moon systems?*

II *How do transfer trajectories in the Sun-Earth system differ from those in the Earth-Moon system?*

III *Which optimization method is most suitable to find time-optimal transfer trajectories between solar-sail displaced libration point orbits in the Sun-Earth and Earth-Moon systems?*

1.4. Report outline

The rest of this report is organized as follows. Chapter 2 presents the main body of the thesis, in the form of a draft journal article. This article contains a complete representation of the work, and can be read independently of the rest of the report. The conclusions are discussed in chapter 3, together with a reflection on the research questions and recommendations for future work. Finally, a verification of the methods and techniques that were used is described in the appendix.

2

Journal Article

Time-Optimal Transfers Between Planar Solar-Sail Libration Point Orbits

Roderick de Boer
Delft University of Technology

This paper presents time-optimal transfer trajectories between planar solar-sail displaced libration point orbits around the L_1 and L_2 points of the Sun-Earth and Earth-Moon systems. Initial guesses for these transfers are generated as two-segment trajectories, with a fixed sail attitude along each segment. The position and velocity discontinuity between the segments is minimized by means of a genetic-algorithm approach. The time of flight of these trajectories is then optimized by means of a direct pseudo-spectral collocation method as well as a multiple shooting differential correction (MSDC) method. The results of these methods are subsequently compared. Pseudo-spectral collocation was found to outperform MSDC in the solar-sail augmented Sun-Earth system, obtaining trajectories with transfer times as short as 101 days. Differential correction generally yields trajectories with slightly longer flight times than pseudo-spectral collocation, but converges more reliably. In the time-dependent solar-sail augmented Earth-Moon system, pseudo-spectral collocation fails to provide reproducible results. Transfer trajectories with flight times as short as 15.6 days are obtained in the Earth-Moon system using MSDC, but these trajectories feature control discontinuities that are likely to be problematic in practice.

I. Introduction

Using solar radiation pressure to propel a spacecraft is a concept that dates back to the early rocket pioneers at the beginning of the 20th century. Some early concrete mission proposals were considered in the 1970s for missions to the outer solar system, but ultimately no solar sail was flown in this era [1]. However, the start of the 21st century has seen a renewed interest in solar sails. The IKAROS mission has demonstrated propulsion and attitude control capabilities while en route to Venus [2], NanoSail-D2 and Lightsail-1 were deployed in Earth orbit [3, 4], and Lightsail-2 has successfully demonstrated Earth-bound orbit raising using solar-sail propulsion [5].

Solar sails are able to provide acceleration without consuming propellant, which provides a unique advantage for certain classes of missions. Spacecraft that are equipped with a solar sail are able to maintain their propulsion capability essentially indefinitely. The acceleration provided by a solar sail allows a spacecraft to maintain non-Keplerian orbits, which can potentially provide scientific observation or communication capabilities which cannot otherwise be achieved [1]. Recent work has found novel solar-sail displaced periodic orbits in the Sun-Earth and Earth-Moon systems. These orbits form extended families of libration point orbits, and Earth-centered orbits have also been found [6–8]. Spacecraft placed in these orbits can be used to provide continuous coverage of the polar regions of the Earth or Moon for observation and communication, monitor for harmful space weather events, and perform space physics research.

By continuously accelerating, a spacecraft equipped with a solar sail is able to reach speeds far in excess of what a conventional chemical or even ion engine can provide. In addition, solar-sail spacecraft potentially have a greater capability to continually transfer between different orbits than spacecraft with conventional propulsion systems. For certain applications this could greatly enhance the value of a mission, by allowing a single spacecraft to provide observations from multiple vantage points over time, which would otherwise require a constellation of multiple spacecraft.

To date, the only example of a transfer between libration point orbits was conducted in NASA's ARTEMIS mission [9]. The objective of this mission was to investigate the effect of the Moon on the magnetic fields of the Earth and Sun by measuring the solar wind at various locations. Twin spacecraft were inserted into quasi-periodic Lissajous orbits around the L_1 and L_2 points of the Earth-Moon system. After a period of initial observations, the L_2 spacecraft was transferred into an L_1 orbit as well. Conventional propulsion methods were used for both station-keeping and insertion into the libration point orbits [10]. A similar future mission could benefit from the unlimited propulsive endurance of a solar sail.

Prior work on solar-sail trajectories has been mainly concerned with finding interplanetary trajectories or Earth-escape trajectories. Transfers between displaced libration point orbits have received less attention. Several papers have investigated transfers to the triangular libration points of the Sun-Earth system. Ref. [11] found transfer trajectories between a low Earth parking orbit and the L_5 point, Ref. [12] investigated transfers from the L_1 and L_2 points to the region of practical stability of the L_4 and L_5 points, and Ref. [13] found trajectories to the L_5 point, departing from solar-sail displaced orbits around the L_1 and L_2 points. Transfers between displaced orbits around the co-linear libration points have not yet been investigated.

Feasible trajectories between high Earth orbit and displaced vertical Lyapunov orbits around the Earth-Moon L_2 points were found by Ref. [14]. Homoclinic and heteroclinic connections between planar displaced orbits around the Earth-Moon L_1 and L_2 points were found by Ref. [15]. These connections depart and arrive along the unstable and stable manifolds of the orbits in question, and were not optimized for time of flight.

This paper will add to the literature by finding time-optimal transfer trajectories between a number of solar-sail displaced libration point orbits around the L_1 and L_2 points of the Sun-Earth and Earth-Moon systems. Two methods for finding these trajectories will be compared: direct pseudospectral collocation, as implemented in the open-source software package PSOPT [16], and multiple shooting with differential correction. Such trajectories have not been studied before, and investigating the nature and control requirements of these trajectories will demonstrate the feasibility of using near-future solar-sail technology to improve the scientific output of future missions similar to ARTEMIS. Furthermore, the framework presented in this paper can be expanded to investigate transfers between a wider range of solar-sail orbits.

II. Dynamics

In the well-known circular restricted three-body problem (CR3BP) the motion of an object P is governed by the gravitational attraction of two primary bodies with mass m_1 and m_2, respectively. The mass of the object is considered to be negligible compared to that of the primary bodies, and is assumed to exert no gravitational influence. Furthermore, the primary bodies are assumed to move in circular orbits about their common center of mass.

The reference frame used to describe the motion of an object P within the framework of the CR3BP is displayed in Fig. 1. An orthogonal reference frame is defined with the centre of mass of the primary bodies as the origin. The x-axis runs along the line connecting the primary bodies, with the positive direction pointing towards m_2, the smaller of the two primary bodies. The z-axis coincides with the angular momentum vector of the orbiting bodies, and the y-axis completes the right-handed reference frame. The reference frame rotates about the z-axis with an angular velocity of $\boldsymbol{\omega} = \omega\hat{\mathbf{z}}$. Within this reference frame, the motion of a spacecraft equipped with a solar sail is governed by [17] :

$$\ddot{\mathbf{r}} + 2\boldsymbol{\omega} \times \dot{\mathbf{r}} + \boldsymbol{\omega} \times (\boldsymbol{\omega} \times \mathbf{r}) = \nabla U + \mathbf{a}_s, \tag{1}$$

where the three terms on the left-hand side are the kinematic, Coriolis and centripetal accelerations respectively, U is the gravitational potential of the primary bodies, and $\mathbf{a}_s$ is the acceleration provided by the solar sail, given by:

$$\mathbf{a}_S = \begin{bmatrix} a_{S,x} & a_{S,y} & a_{S,z} \end{bmatrix}^T. \tag{2}$$

Equation 1 is made dimensionless by introducing new units of time, mass, and length. As the unit for mass, the sum of the primary body masses $(m_1 + m_2)$ is used. The unit for length is defined as the distance between the primaries, and the reciprocal of the angular velocity of the reference frame $1/\omega$ is used as the unit of time. If μ is then defined as the fraction of the mass of the smaller primary body, m_2, with respect to the total system mass, the x coordinates of the primary bodies become $-\mu$ and $1 - \mu$, respectively. The value of μ is equal to 3.0035×10^{-6} for the Sun-Earth system, and 0.01215 for the Earth-Moon system. The gravitational potential U is then given by:

$$U = -\left(\frac{1-\mu}{r_1} + \frac{\mu}{r_2}\right), \tag{3}$$

where r_1 and r_2 are the distances between the spacecraft and the primary bodies, given by $r_1 = \sqrt{(\mu + x)^2 + y^2 + z^2}$ and $r_2 = \sqrt{(1 - \mu - x)^2 + y^2 + z^2}$, respectively. The transfer trajectories that are investigated in this work are between planar

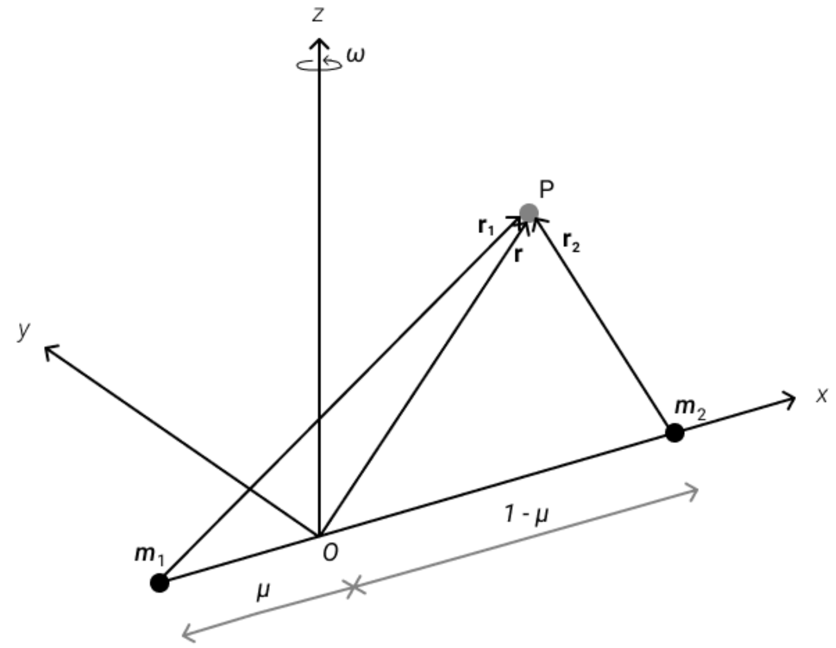

Fig. 1 Definition of the CR3BP reference frame.

Lyapunov orbits in the xy plane, as presented in Section III. The out-of-plane motion can therefore be omitted, and Eq. 1 can be decomposed into scalar acceleration components [17]:

$$\begin{aligned} \ddot{x} &= -\frac{1-\mu}{r_1^3}(\mu + x) + \frac{\mu}{r_2^3}(1-\mu-x) + 2\dot{y} + x + a_{s,x}, \\ \ddot{y} &= -\frac{1-\mu}{r_1^3}y - \frac{\mu}{r_2^3}y - 2\dot{x} + y + a_{s,y}, \end{aligned} \tag{4}$$

A. Solar-Sail Force Model

The solar-sail force model adopted in this paper assumes an idealized solar sail, which provides perfect specular reflection of the incoming solar radiation. For such a sail, the resulting acceleration is directed along the solar-sail normal vector $\hat{\mathbf{n}} = [n_x, n_y]^T$, as shown in the left panel of Fig. 2. More complicated sail force models account for partly diffuse reflection, sail billowing, and degradation [1, 18, 19], but these effects are not considered in this work.

The magnitude of the solar-sail acceleration depends on the sail area, spacecraft mass, and the distance from the Sun. Because both the solar radiation pressure and the gravitational attraction of the Sun are inversely proportional to the square of the distance to the Sun, it is convenient to express the solar-sail acceleration as a fraction of the solar gravitational acceleration through the solar-sail lightness number β. A feasible near-future value for the solar-sail lightness number is 0.04 [20, 21], which corresponds to an acceleration of 0.239 mm/s^2 for a sail directly facing the

Sun, at a distance of one AU. The dimensionless acceleration provided by the solar sail can then be expressed as [1]:

$$\mathbf{a}_s = \beta \frac{1-\mu}{{r_1}^2} (\hat{\mathbf{S}} \cdot \hat{\mathbf{n}})^2 \, \hat{\mathbf{n}}, \tag{5}$$

where the Sun-line $\hat{\mathbf{S}}$ is the unit vector pointing from the Sun to the solar sail.

In the Sun-Earth system, the Sun-line $\hat{\mathbf{S}}$ is co-linear with $\mathbf{r}_1$. The orientation of the solar sail with respect to the Sun-line can be expressed using the cone angle α, as shown in Fig. 2. The sail acceleration is then given by:

$$\mathbf{a}_{s,SE} = \beta \frac{1-\mu}{{r_1}^2} \cos^2\alpha \, \hat{\mathbf{n}}, \tag{6}$$

where the subscript SE is used throughout this paper to refer to cases in the Sun-Earth system.

In the Earth-Moon system, the position of the Sun is no longer fixed. From the perspective of the Earth-Moon reference frame, the Sun rotates around the system in clockwise direction with an angular rate of Ω_S, as depicted in the right panel of Fig. 2. In non-dimensional units, Ω_S is equal to 0.9252. Unlike the Sun-Earth system, the apparent motion of the Sun makes the solar-sail augmented Earth-Moon system non-autonomous. Throughout this paper, the position of the Sun is assumed to be along the negative x-axis at time $t = 0$. The inclination between the orbital planes of the Moon around the Earth and the Earth around the Sun is assumed to be zero. The Sun-line vector over time is then given by [7]:

$$\hat{\mathbf{S}}_{EM} = \begin{bmatrix} \cos(\Omega_S t) \\ -\sin(\Omega_S t) \end{bmatrix}, \tag{7}$$

where the subscript EM is used throughout this paper to refer to cases in the Earth-Moon system.

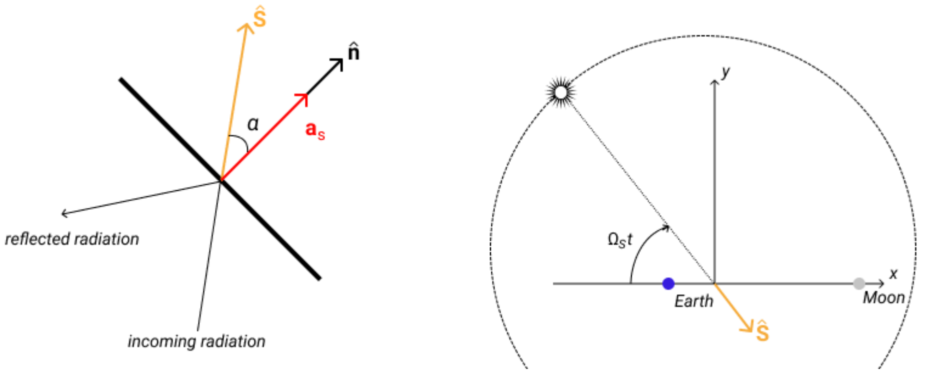

Fig. 2 Solar sail force model: acceleration of reflecting sail (left) and definition of the Sun-line in the Earth-Moon system (right).

In the Earth-Moon system, variations in solar radiation pressure due to changes in the distance between the sail and the Sun are small. The solar radiation pressure is therefore assumed to be constant, and equal to the solar radiation pressure at a distance of one AU from the Sun. The first two terms on the right hand side of Eq. 5 can then be replaced with a characteristic sail acceleration $a_{0,EM}$. A solar-sail lightness number of $\beta = 0.04$ corresponds to an $a_{0,EM}$ value of 0.09. The solar-sail acceleration in the Earth-Moon systems is then given by:

$$\mathbf{a}_{s,EM} = a_{0,EM} (\hat{\mathbf{S}}_{EM} \cdot \hat{\mathbf{n}})^2 \, \hat{\mathbf{n}}. \tag{8}$$

III. Optimal Control Problem

The aim of this work is to find time-optimal transfer trajectories between a number of solar-sail displaced libration point orbits in the Sun-Earth and Earth-Moon systems by solving the associated optimal control problem. The objective of an optimal control problem is to find a state history $\mathbf{x}(t)$ and a control history $\mathbf{u}(t)$ that minimizes a cost function J, which in general terms is defined as [22]:

$$J = G(\mathbf{x}_0, \mathbf{x}_f, t_0, t_f, \mathbf{p}) + \int_{t_0}^{t_f} L(\mathbf{x}(t), \mathbf{u}(t), t) dt, \tag{9}$$

where $\mathbf{p}$ is a vector of static optimization parameters, and the subscripts 0 and f refer to the initial and final states, respectively.

The solution must satisfy the system dynamics:

$$\dot{\mathbf{x}}(t) = \mathbf{f}(\mathbf{x}(t), \mathbf{u}(t), t), \tag{10}$$

as well as a set of constraints:

$$\mathbf{c}(\mathbf{x}, \mathbf{u}, t) \leq 0. \tag{11}$$

In this paper, the time of flight of the transfer trajectories will be optimized. The cost function in Eq. 9 thus reduces to:

$$J = t_f - t_0. \tag{12}$$

The state vector $\mathbf{x}(t)$ consists of the spacecraft's position and velocity in Cartesian components:

$$\mathbf{x} = \begin{bmatrix} x & y & \dot{x} & \dot{y} \end{bmatrix}^T. \tag{13}$$

The control consists of the solar-sail cone angle: $\mathbf{u}(t) = \alpha(t)$. Because it is physically impossible for a solar sail to generate a force with a component in the direction of the source of the radiation, the angle is constrained to a semicircle facing away from the Sun: $-90° \leq \alpha \leq 90°$. The boundary conditions for the state vector are determined by the arrival and departure points along the libration point orbits. The starting condition $\mathbf{x}_0$ is obtained by propagating the departure orbit from time T_0 to a certain time along the orbit T^*_{dep}, as illustrated in Fig. 3. The same is done for the end state $\mathbf{x}_f$, by propagating the arrival orbit from T_0 to T^*_{arr}. In the Sun-Earth system, T^*_{dep} and T^*_{arr} can be independently selected, but this is not the case for the Earth-Moon system. This is because the position of the Sun is an implicit component of the orbit state, and in the Earth-Moon system the position of the Sun is not constant. Therefore, a restriction is applied to T^*_{dep} and T^*_{arr}:

$$T^*_{arr} = T^*_{dep} + TF, \tag{14}$$

where TF is the time of flight of the transfer trajectory.

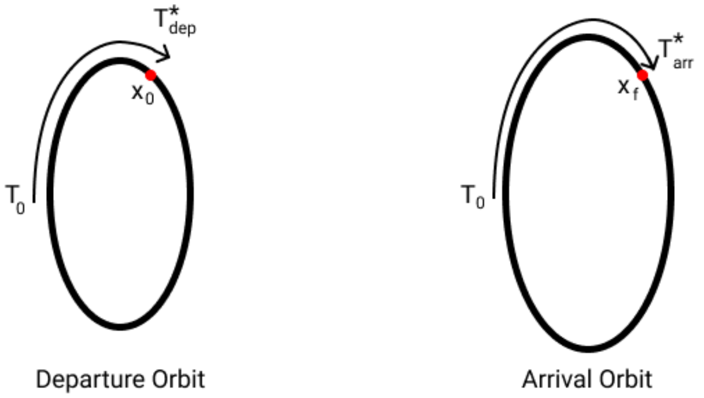

Fig. 3 State vector boundary conditions for the optimal control problem.

Bounds are set on the state variables to ensure that the trajectory remains close to the target orbits:

$$\left.\begin{aligned} 0.9 \le x \le 1.1 \\ -0.1 \le y \le 0.1 \end{aligned}\right\} Sun - Earth$$
$$\left.\begin{aligned} 0 \le x \le 2 \\ -1 \le y \le 1 \end{aligned}\right\} Earth - Moon \tag{15}$$

The difference between the bounds of the Sun-Earth and Earth-Moon systems reflects the scale difference between the size of the libration point orbits in those systems. In the Earth-Moon system, $0 \le t_0 = T^*_{dep} \le P_{dep}$ and $0 \le t_f = T^*_{arr} \le 2P_{max}$, where P_{dep} is the period of the departure orbit, and P_{max} is the period of either the departure or arrival orbit, whichever is larger. In the Sun-Earth system, the times along the departure and arrival orbits are independent of each other, so $t_0 = 0$ and $0 \le t_f \le 2P_{max}$.

A. Orbit Sets

Several different families of periodic orbits exist around the libration points of the CR3BP. These families include planar and vertical Lyapunov orbits, halo orbits, and quasi-periodic Lissajous orbits [23, 24]. These classical orbits can be extended through the addition of a solar-sail acceleration. Families of solar-sail displaced halo and Lyapunov orbits have been found in the Sun-Earth system [13] as well as the Earth-Moon system [7]. Starting from a classical orbit, a periodic orbit for a sail with very low performance can be found by applying a differential correction scheme [7]. Orbits for sails with greater performance are then found by using the differential corrector in a continuation process, where the sail performance is gradually increased in each iteration [7]. The sail is controlled through a simple steering law. For the Sun-Earth case, the work in [13] assumed that the sail normal vector is always aligned with the Sun-line: $\hat{\mathbf{n}} = \hat{\mathbf{S}}$. In the Earth-Moon case, Ref. [7] also considered an additional steering law where the sail is aligned with the Earth-Moon line, with the sail normal vector given by:

$$\hat{\mathbf{n}} = sign(\cos(\Omega_S t)) \begin{bmatrix} 1 & 0 \end{bmatrix}^T, \tag{16}$$

where the $sign(\cos(\Omega_S t)$ term represents the direction of the sail acceleration switching between the positive and negative x-axis as the Sun moves around the system. From the substitution of Eqs. 7 and 16 into Eq. 8 it is clear that the Sun-line steering law provides a constant acceleration magnitude with variable acceleration direction, whereas the Earth-Moon steering law provides a constant acceleration direction with variable magnitude.

To demonstrate the capability of solar-sail propulsion to transfer between libration point orbits, this paper will design transfer trajectories between four orbits in each system; two around L_1 and two around L_2. All orbits considered are planar Lyapunov orbits. The characteristics of these orbits are presented in Table 1 for the Sun-Earth system, obtained from Ref. [13], and in Table 2 for the Earth-Moon system, obtained from Ref. [7]. Note that the periods of the Sun-Earth system orbits vary, whereas all Earth-Moon orbits have the same period. For a solar-sail orbit to be periodic in the Earth-Moon system, the period has to be an integer fraction or multiple of the period of the apparent orbit of the Sun around the system. The orbits considered in this work all have a period equal to that of the Sun. All orbits are displayed in Fig. 4.

Table 1 Characteristics of selected periodic orbits in the Sun-Earth system.

Orbit	β	Period	Steering Law	Initial State
SE-L1A	0.04	5.2669	Sun-line	[0.975130; 0.000012; 0.000008; 0.021762]
SE-L1B	0.04	6.0046	Sun-line	[0.969703; -0.000017; -0.000009; 0.033174]
SE-L2A	0.04	2.1321	Sun-line	[0.995271; 0.007389; -0.000212; 0.011473]
SE-L2B	0.04	2.3307	Sun-line	[1.003331; 0.000064; 0.000432; -0.046171]

Table 2 Characteristics of selected periodic orbits in the Earth-Moon system.

Orbit	$a_{0,EM}$	Period	Steering Law	Initial State
EM-L1A	0.1	6.7912	Earth-Moon line	[0.785751; 0; 0; 0.361937]
EM-L1B	0.1	6.7912	Sun-line	[0.906177; 0; 0; -0.443959]
EM-L2A	0.1	6.7912	Earth-Moon line	[1.168131; 0; 0; -0.169859]
EM-L2B	0.1	6.7912	Sun-line	[1.174760 ; 0; 0; -0.244425]

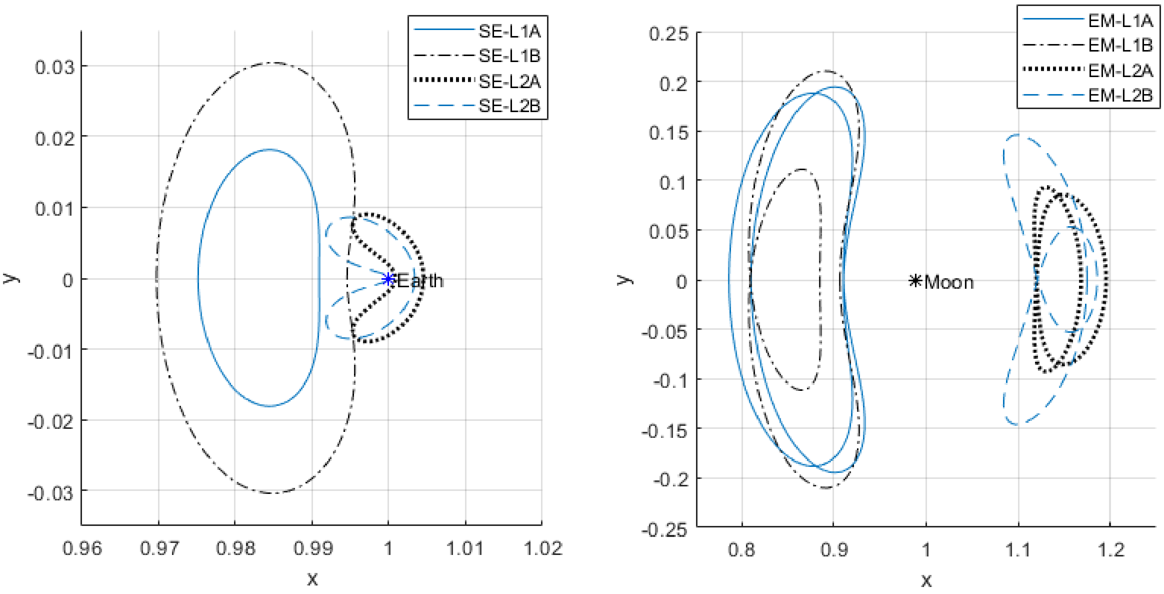

Fig. 4 Solar-sail displaced Lyapunov orbits in the Sun-Earth system (left) and Earth-Moon system (right).

IV. Methodology

Two methods are used to solve the optimal control problem presented in section III. A direct pseudo-spectral collocation method, as implemented by the open source software package PSOPT, is introduced in section IV.A. Secondly, section IV.B describes a method employing multiple shooting with differential correction. Both methods require an initial guess to start the optimization procedure. Initial guess trajectories to start the optimization process are obtained through a genetic-algorithm approach, as described in section IV.C.

A. Pseudo-spectral Collocation

The first technique used to solve the optimal control problem is a direct pseudo-spectral collocation method, as implemented by the software package PSOPT [16]. The trajectory is discretized into a grid of nodes, and the value of all time-dependent variables are approximated between the nodes by Legendre polynomials. Differentiation of these polynomials can be achieved my matrix multiplications only, and integrals are approximated using Gauss quadrature rules. Locally optimal solutions can then be found using non-linear programming (NLP) techniques, making use of the IPOPT NLP solver [25]. A maximum tolerance of 1×10^{-5} was used for the NLP convergence tolerance, but where possible stricter tolerances were set to obtain more accurate trajectories. The boundary conditions of the transfer trajectory are obtained by interpolating from a table of departure and arrival orbit states. Static optimization parameters representing the time along the orbit are used for this interpolation for transfers in the Sun-Earth system, as described in section III, whereas the start and end times of the trajectories are used in the time-dependent Earth-Moon system. Interpolating from a table of orbit states requires PSOPT to use numerical differentiation, which is less accurate and slower than using automatic differentiation [26].

B. Differential Corrector

The differential correction method presented in this section largely follows the approach in Ref. [27], but accounting for the solar-sail acceleration. The differential corrector starts by dividing the initial guess trajectory into $n - 1$ segments, with n nodes. The generation of this initial guess trajectory will be discussed in section IV.C. The position and velocity at each node are interpolated from the integrated initial guess trajectory based on the epoch of the node. Each node i has an augmented state vector associated to it, defined as:

$$\mathbf{X}_i = \begin{bmatrix} x & y & \dot{x} & \dot{y} & \alpha \end{bmatrix}^T . \tag{17}$$

Along the trajectory segment between nodes i and $i + 1$, the cone angle α is assumed to be constant, and equal to the cone angle value at node i. The differential corrector transforms the infeasible initial guess into a continuous trajectory with a two-phase method. The first phase, or *level one*, of the differential corrector employs sequential single shooting for each trajectory segment. The objective of the level one differential corrector is to obtain a trajectory that is continuous in time and position, by introducing discrete ΔVs at the nodes. In the second phase, or *level two*, the epochs, positions, and cone angles of each node are adjusted simultaneously to minimize these ΔVs.

Level one differential corrector

The effect of small changes to the state at time t_0 to the state at a later time t can be expressed by the state transition matrix (STM) :

$$\Phi(t, t_0) = \frac{\delta \mathbf{X}(t)}{\delta \mathbf{X}(t_0)}. \tag{18}$$

The STM is obtained by propagating it along with the state vector from an initial condition of $\Phi(t_0, t_0) = I$ using the relation:

$$\dot{\Phi}(t, t_0) = A(t)\Phi(t, t_0), \tag{19}$$

where the matrix A is defined as:

$$A(t) = \frac{\delta \dot{\mathbf{X}}(t)}{\delta \mathbf{X}(t)}. \tag{20}$$

Changes in the state vector at time t as a result of small perturbations to the state vector at time t_0 are then given by:

$$\delta \mathbf{X}_t = \Phi(t, t_0)\Delta \mathbf{X}_0. \tag{21}$$

The state vector in Eq. 17 can be decomposed into a position vector $\mathbf{R} = [x, y]^T$, a velocity vector $\mathbf{V} = [\dot{x}, \dot{y}]^T$, and the cone angle α. Equation 21 can be expanded in terms of these sub-components [27]:

$$\begin{bmatrix} \delta \mathbf{R}_t \\ \delta \mathbf{V}_t \\ \delta \alpha_t \end{bmatrix} = \begin{bmatrix} \Phi_{RR}(t, t_0) & \Phi_{RV}(t, t_0) & \Phi_{R\alpha}(t, t_0) \\ \Phi_{VR}(t, t_0) & \Phi_{VV}(t, t_0) & \Phi_{V\alpha}(t, t_0) \\ \Phi_{\alpha R}(t, t_0) & \Phi_{\alpha V}(t, t_0) & \Phi_{\alpha\alpha}(t, t_0) \end{bmatrix} \begin{bmatrix} \Delta \mathbf{R}_0 \\ \Delta \mathbf{V}_0 \\ \Delta \alpha_0 \end{bmatrix}. \tag{22}$$

Starting with the first node, the trajectory segment is propagated from the initial conditions at node i ($\mathbf{R}_i, \mathbf{V}_i, t_i$) to t_{i+1}, the time of the next node. The position error $\delta \mathbf{R}_{i+1}$ is defined as the difference between the position at the end of the propagated segment and the position at the next node, $\mathbf{R}_{i+1}$. Keeping the position and cone angle at node i unchanged, a ΔV is introduced at node i in order to minimize the position error, given by:

$$\Delta \mathbf{V}_i = [\Phi_{RV}(t_{i+1}, t_i)]^{-1} \delta \mathbf{R}_{i+1}. \tag{23}$$

This ΔV is then added to the state vector at node i, which is then again propagated to t_{i+1}. Because Eq. 23 is based on linearized equations of motion, this process is repeated iteratively until the position error at t_{i+1} falls below a set tolerance. A tolerance of 1×10^{-8} was used as the convergence criterion for the level one corrector. The same process is applied to each trajectory segment in succession, resulting in a vector of $\Delta \mathbf{V}$s:

$$\Delta \mathbf{V} = \begin{bmatrix} \Delta \mathbf{V}_1 & \Delta \mathbf{V}_2 & \dots & \Delta \mathbf{V}_n \end{bmatrix}^T \tag{24}$$

Level two differential corrector

The level one differential corrector provides a trajectory that is continuous in time and position, with discrete ΔVs at the node points. Small changes in the ΔV at node i can be approximated as a function of deviations in the position, time, and cone angle of the node itself and of the two adjacent nodes:

$$\delta\Delta\mathbf{V}_i = \begin{bmatrix}\varphi_{i,i-1} & \varphi_{i,i} & \varphi_{i,i+1}\end{bmatrix}\begin{bmatrix}\delta\mathbf{R}_{i-1} & \delta t_{i-1} & \delta\alpha_{i-1} & \delta\mathbf{R}_i & \delta t_i & \delta\alpha_i & \delta\mathbf{R}_{i+1} & \delta t_{i+1} & \delta\alpha_{i+1}\end{bmatrix}^T, \tag{25}$$

where $\varphi_{i,j}$ is a matrix of the partial derivatives of the ΔV at node i with respect to the position, time, and cone angle of node j:

$$\varphi_{i,j} = \begin{bmatrix}\frac{\delta\Delta\mathbf{V}_i}{\delta\mathbf{R}_j} & \frac{\delta\Delta\mathbf{V}_i}{t_j} & \frac{\delta\Delta\mathbf{V}_i}{\delta\alpha_j}\end{bmatrix}. \tag{26}$$

The expression in Eq. 25 can be extended to the whole system of n nodes:

$$\begin{bmatrix}\delta\Delta\mathbf{V}_2 \\ \vdots \\ \delta\Delta\mathbf{V}_{n-1}\end{bmatrix} = M\begin{bmatrix}\delta\mathbf{R}_1 & \delta t_1 & \delta\alpha_1 & \dots & \delta\mathbf{R}_n & \delta t_n & \delta\alpha_n\end{bmatrix}^T, \tag{27}$$

with M defined as:

$$M = \begin{bmatrix}\varphi_{2,1} & \varphi_{2,2} & \varphi_{2,3} & 0 & 0 & \dots & 0 \\ 0 & \varphi_{3,2} & \varphi_{3,3} & \varphi_{3,4} & 0 & \dots & 0 \\ \vdots & \vdots & \vdots & & \ddots & & \vdots \\ 0 & 0 & 0 & \dots & \varphi_{n-1,n-2} & \varphi_{n-1,n-1} & \varphi_{n-1,n}\end{bmatrix}. \tag{28}$$

Because each node is assumed to depend only on its two immediate neighbours, the matrix M is sparsely populated along the diagonal. The linear system displayed in Eq. 27 is undetermined, because there are $n-2$ equations and $3n$ unknowns, and can therefore not be directly solved. A guess for the changes in node positions, times and cone angles that reduce the $\Delta\mathbf{V}$s at the nodes is obtained by [27]:

$$\begin{bmatrix} \delta\mathbf{R}_1 \\ \delta t_1 \\ \delta\alpha_1 \\ \vdots \\ \delta\mathbf{R}_n \\ \delta t_n \\ \delta\alpha_n \end{bmatrix} = M^T (MM^T)^{-1} \begin{bmatrix} \delta\Delta\mathbf{V}_2 \\ \vdots \\ \delta\Delta\mathbf{V}_{n-1} \end{bmatrix}. \tag{29}$$

After the node update step in Eq. 29 the trajectory is no longer continuous. The level one and level two correctors are therefore applied iteratively, until the ΔVs produced by the level one corrector fall below a set tolerance. In this work, the differential corrector is considered to have converged on a solution if the individual position errors at the nodes fall below 1×10^{-8}, as mentioned in the section deriving the level one corrector, and the norm of the vector $\Delta\mathbf{V}$ produced by the level one corrector falls below 1×10^{-6}.

The partial derivatives in Eq. 26 can be constructed by setting up linearized relations between the respective variables, using the STMs obtained by the level one corrector. To illustrate this process, consider a trajectory composed of two segments and three nodes, as depicted in Fig. 5. The ΔV at node two is defined as:

$$\Delta\mathbf{V}_2 = \mathbf{V}_2^+ - \mathbf{V}_2^-, \tag{30}$$

where $\mathbf{V}_2^-$ is the velocity at the end of the first trajectory segment, and $\mathbf{V}_2^+$ is the velocity at the start of the second trajectory segment. There are no discontinuities in epoch, and the level one corrector eliminated the discontinuities in position, so $t_2^+ = t_2^- = t_2$ and $\mathbf{R}_2^+ = \mathbf{R}_2^- = \mathbf{R}_2$.

The STM relations in Eq. 22 can be further expanded by also including changes in the positions and velocities due to small changes in the epochs of the nodes. For the trajectory segment between nodes one and two, this yields [27]:

$$\begin{bmatrix} \delta\mathbf{R}_2^- - \mathbf{V}_2^-\delta t_2^- \\ \delta\mathbf{V}_2^- - \mathbf{a}_2^-\delta t_2^- \\ \delta\alpha_2^- \end{bmatrix} = \begin{bmatrix} \Phi_{RR}(t_2,t_1) & \Phi_{RV}(t_2,t_1) & \Phi_{R\alpha}(t_2,t_1) \\ \Phi_{VR}(t_2,t_1) & \Phi_{VV}(t_2,t_1) & \Phi_{V\alpha}(t_2,t_1) \\ \Phi_{\alpha R}(t_2,t_1) & \Phi_{\alpha V}(t_2,t_1) & \Phi_{\alpha\alpha}(t_2,t_1) \end{bmatrix} \begin{bmatrix} \Delta\mathbf{R}_1^+ - \mathbf{V}_1^+\delta t_1^+ \\ \Delta\mathbf{V}_1^+ - \mathbf{a}_1^+\delta t_1^+ \\ \Delta\alpha_1^+ \end{bmatrix}. \tag{31}$$

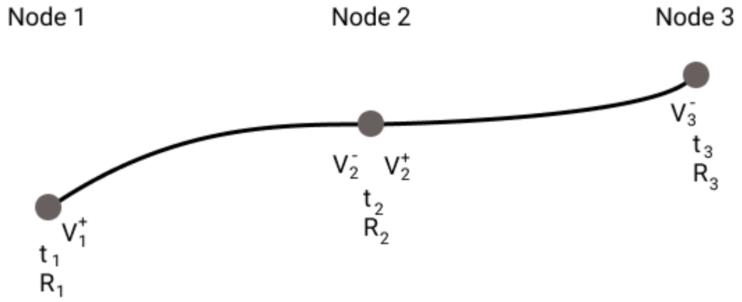

Fig. 5 Positions, epochs and velocities of nodes and segments in the level two corrector.

Additionally, the inverse relation can be used, which is given by:

$$\begin{bmatrix} \delta\mathbf{R}_1^+ - \mathbf{V}_1^+\delta t_1^+ \\ \delta\mathbf{V}_1^+ - \mathbf{a}_1^+\delta t_1^+ \\ \delta\alpha_1^+ \end{bmatrix} = \begin{bmatrix} \Phi_{RR}(t_1,t_2) & \Phi_{RV}(t_1,t_2) & \Phi_{R\alpha}(t_1,t_2) \\ \Phi_{VR}(t_1,t_2) & \Phi_{VV}(t_1,t_2) & \Phi_{V\alpha}(t_1,t_2) \\ \Phi_{\alpha R}(t_1,t_2) & \Phi_{\alpha V}(t_1,t_2) & \Phi_{\alpha\alpha}(t_1,t_2) \end{bmatrix} \begin{bmatrix} \delta\mathbf{R}_2^- - \mathbf{V}_2^-\delta t_2^- \\ \delta\mathbf{V}_2^- - \mathbf{a}_2^-\delta t_2^- \\ \delta\alpha_2^- \end{bmatrix}. \tag{32}$$

The STM $\Phi(t_2, t_1)$ is obtained from the level one corrector, and $\Phi(t_1, t_2)$ can be obtained by $\Phi(t_1, t_2) = \Phi(t_2, t_1)^{-1}$. Note that only the complete STM can be obtained in this way, as this does not hold for the individual sub-components. Similar equations can be set up for the relation between nodes two and three. Partial derivatives of $\Delta\mathbf{V}_2$ with respect to the other variables can then be constructed. As an example, from Eqs. 30 and 32 it is clear that:

$$\frac{\delta\Delta\mathbf{V}_2}{\delta\mathbf{R}_1} = -\frac{\delta\mathbf{V}_2^-}{\delta\mathbf{R}_1^+} = \Phi_{RV}(t_1,t_2)^{-1}. \tag{33}$$

Similarly:

$$\frac{\delta\Delta\mathbf{V}_2}{\delta t_1} = -\frac{\delta\mathbf{V}_2^-}{\delta t_1^+} = \Phi_{RV}(t_1,t_2)^{-1}\mathbf{V}_1^+. \tag{34}$$

Partial derivatives for the other variables are constructed in a similar way. This procedure is carried out for all internal nodes to populate the matrix M.

Differential corrector constraints

Constraints can be placed on the level two corrector by modifying Eq. 27 by appending the vector $\Delta\mathbf{V}$ with the constraint values and augmenting the M matrix [27]:

$$
\begin{bmatrix} \delta\Delta\mathbf{V}_2 \\ \vdots \\ \delta\Delta\mathbf{V}_{n-1} \\ \delta\mathbf{c} \end{bmatrix} = \begin{bmatrix} M \\ C \end{bmatrix} \begin{bmatrix} \delta\mathbf{R}_1 & \delta t_1 & \delta\alpha_1 & \dots & \delta\mathbf{R}_n & \delta t_n & \delta\alpha_n \end{bmatrix}^T, \tag{35}
$$

where $\mathbf{c}$ is a vector of constraints, and C is a matrix of the partial derivatives of the individual constraints with respect to the node positions, epochs, and cone angles. This matrix C is analogous to the M matrix for the original $\Delta\mathbf{V}$ vector, as specified by Eq. 28, and is constructed in a similar way. Each constraint acts on a single node, but multiple constraints may act on the same node. Furthermore, as was the case with $\Delta\mathbf{V}$, only directly adjacent node states are assumed to have influence on the constraint value.

Partial derivatives of the constraints are constructed in a similar way to the partial derivatives of the $\Delta\mathbf{V}$ vector, but the constraints may also be a function of velocity. This is accounted for by making use of the chain rule. As an example, the partial derivative of a constraint with respect to the position of the node upon which the constraint acts is given by [27]:

$$
\frac{\delta c_{i,k}}{\delta \mathbf{R}_i} = \frac{\delta c_{i,k}}{\delta \mathbf{R}_i} + \frac{\delta c_{i,k}}{\delta \mathbf{V}_i^-}\frac{\delta \mathbf{V}_i^-}{\delta \mathbf{R}_i} + \frac{\delta c_{i,k}}{\delta \mathbf{V}_i^+}\frac{\delta \mathbf{V}_i^+}{\delta \mathbf{R}_i}, \tag{36}
$$

where $c_{i,k}$ refers to the k-th constraint acting on node i. For the problem considered in this paper, four types of constraint are applied. These constraints are introduced hereafter.

Endpoint constraints

Position and velocity constraints are applied to the first and last nodes:

$$
\begin{aligned} \mathbf{X}_1 - \mathbf{X}_d(T_{dep}^*) &= 0 \\ \mathbf{X}_n - \mathbf{X}_a(T_{arr}^*) &= 0 \end{aligned} \tag{37}
$$

where $\mathbf{X}_d(t)$ and $\mathbf{X}_a(t)$ are Fourier-series approximations of the arrival and departure orbit states as a function of time. Approximating the target orbits with Fourier series allows for the straightforward computation of the partial derivatives of the boundary conditions with respect to time. For transfers in the Earth-Moon system, $T_{dep}^* = t_1$ and $T_{arr}^* = t_n$. In the case of transfers in the Sun-Earth system, the required departure and arrival times can be independently chosen along the target orbits, as described in Section III. Therefore, T_{dep}^* and T_{arr}^* are included as independent optimization variables. For Sun-Earth system transfers these variables are appended to the vector of position, epoch, and cone angle deviations on the right-hand side of Eq. 35.

Epoch constraints

The epoch of each node is adjusted by the differential corrector independently of the epochs of the other nodes. Left unconstrained, this can result in trajectory segments going backwards in time. Furthermore, the convergence of the algorithm is improved when nodes remain equally spaced in time [27]. Because the differential corrector can only apply equality constraints, these two concerns are addressed simultaneously by formulating a combined constraint for each node except the last:

$$(t_{i+1} - t_i) - \frac{t_n - t_1}{n - 1} = 0, \quad i = 1, 2, ..., n - 1. \tag{38}$$

This constraint ensures that the difference in epochs between two adjacent nodes is equal to the total flight time divided by the number of segments, providing equally spaced, sequential nodes.

Cone angle constraints

As mentioned in section III, the solar sail cannot generate an acceleration with a component in the direction of the Sun. The cone angle should therefore be constrained to the interval $-90° \leq \alpha \leq 90°$. The differential corrector cannot naturally enforce this inequality constraint. The bounds on the cone angle are therefore enforced by resetting the cone angle to 90° or −90° after the node update in Eq. 29 is applied if the cone angle at a node would otherwise exceed these values.

Continuation constraint

The differential corrector scheme presented in this section produces feasible trajectories by driving the constraint values to zero, but cannot optimize the trajectory. The time of flight of a converged trajectory can be reduced however, by applying the differential corrector in a continuation scheme. After a feasible trajectory has been obtained, the differential corrector is applied again with an additional constraint, given by:

$$t_n - t_1 - T^* - \delta T^* = 0, \tag{39}$$

where T^* is the time of flight of the previously converged trajectory, and δT^* is a small time increment. The converged trajectory is used as the initial guess for the new iteration. This process is repeated until the differential corrector no longer converges.

Finally, it should be noted that this method is based on linearizing the dynamics of a highly non-linear system. The node update produced by Eq. 29 can yield changes in node position, time, or cone angle that are far beyond the range where this linearized approximation is accurate, resulting in a rapidly diverging trajectory. A limit of 0.02 is therefore set on the maximum change in the node position $||\mathbf{R}||$ that is allowed in a single iteration. If this limit is exceeded by any node, a scaling factor is applied to the entire node update vector.

C. Initial Guess Trajectories

An initial guess is required to start the optimization process. A diagram of the initial guess trajectory generation is displayed in Fig. 6. An initial guess for the transfer is obtained by dividing the transfer trajectory in a departure and arrival phase. The state vector at the start of the departure phase is obtained by interpolating the orbit state at a certain departure time, T^*_{dep}, along the departure orbit. The trajectory is then propagated for a certain length of time, TF_{dep} with a fixed cone angle α_{dep}. The same is done for the arrival trajectory, but this trajectory is propagated backwards in time from a targeted state along the arrival orbit at T^*_{arr} for a length of time equal to TF_{arr}, with fixed cone angle α_{arr}. The mismatch in position and velocity between the end of the departure segment and the beginning of the arrival segment is then minimized by means of a genetic algorithm, as implemented by the *ga.m* routine in MATLAB®. For the Sun-Earth system, the genetic algorithm decision vector is defined as:

$$\mathbf{g}_{SE} = \begin{bmatrix} T^*_{dep} & T^*_{arr} & TF_{dep} & TF_{arr} & \alpha_{dep} & \alpha_{arr} \end{bmatrix}, \tag{40}$$

where the subscripts dep and arr refer to the departure and arrival trajectory segment, respectively. The bounds on the parameters are defined as:

$$\begin{bmatrix} 0 \\ 0 \\ 0 \\ 0 \\ -90^\circ \\ -90^\circ \end{bmatrix} \leq \begin{bmatrix} T^*_{dep} \\ T^*_{arr} \\ TF_{dep} \\ TF_{arr} \\ \alpha_{dep} \\ \alpha_{arr} \end{bmatrix} \leq \begin{bmatrix} P_{dep} \\ P_{arr} \\ P_{max} \\ P_{max} \\ 90^\circ \\ 90^\circ \end{bmatrix}, \tag{41}$$

where P_{dep} is the period of the departure orbit, P_{arr} is de period of the arrival orbit, and P_{max} is the larger of those two periods.

In the Sun-Earth system, the time along the departure and arrival orbits and the flight times of the departure and arrival segments of the transfer trajectory can be independently selected. In the non-autonomous Earth-Moon system however, the position of the Sun, which is dependent on time, must be consistent throughout the entire trajectory. The departure and arrival segments are therefore propagated from their time-dependent starting conditions at T^*_{dep} and T^*_{arr} to an intermediate epoch T^*_{con}, again with constant cone angles α_{dep} and α_{arr}. The genetic algorithm decision vector then becomes:

$$\mathbf{g}_{EM} = \begin{bmatrix} T^*_{dep} & T^*_{con} & T^*_{arr} & \alpha_{dep} & \alpha_{arr} \end{bmatrix}, \tag{42}$$

with bounds defined as:

$$\begin{bmatrix} 0 \\ 0 \\ 0 \\ -90^\circ \\ -90^\circ \end{bmatrix} \leq \begin{bmatrix} T^*_{dep} \\ T^*_{con} \\ T^*_{arr} \\ \alpha_{dep} \\ \alpha_{arr} \end{bmatrix} \leq \begin{bmatrix} P_{dep} \\ 2P_{max} \\ 2P_{max} \\ 90^\circ \\ 90^\circ \end{bmatrix}. \tag{43}$$

A constraint is applied to the parameters to ensure that $T^*_{dep} < T^*_{con} < T^*_{arr}$.

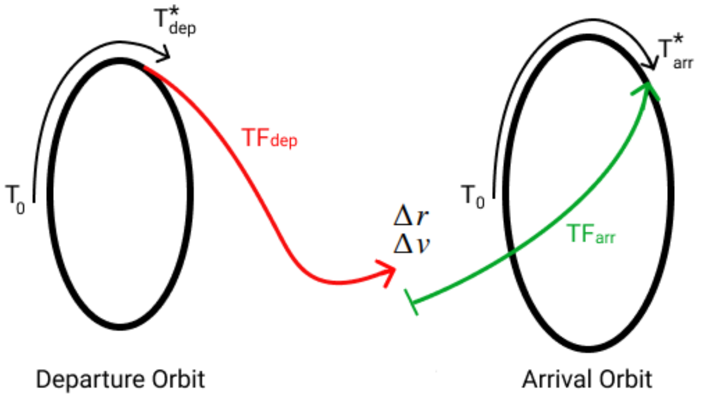

Fig. 6 Generation of initial guess trajectories in the Sun-Earth system using a genetic algorithm.

The cost function of the genetic algorithm is given by:

$$J_{GA} = \Delta r + w_v \Delta v, \tag{44}$$

where Δr and Δv are the position and velocity discontinuities, respectively, and w_v is a weight factor for the velocity discontinuity. There is no a priori guidance on the preferred ratio to trade off position and velocity errors. A velocity weight factor of 0.3 was found to produce initial guess trajectories with small overall errors. For both the Sun-Earth and Earth-Moon cases the total flight time of the initial guess trajectories was constrained to a maximum of twice the period of the departure or arrival orbit, whichever is larger.

For each of the transfers the genetic algorithm is run five times with different RNG seeds, with a population size of 200. The best performing trajectory out of these five seeds is then interpolated along a grid with Legendre-Gauss-Lobatto

(LGL) node spacing for use in PSOPT, or with equally spaced nodes when used an an initial guess for the differential corrector. The properties of the resulting initial guess trajectories are displayed in Table 3 for the Sun-Earth system transfers and in Table 4 for the Earth-Moon system transfers. In the Sun-Earth system, the genetic algorithm is able to generate initial guess trajectories with small position and velocity discontinuities between the departure and arrival segments. Position errors vary from 91 m to 876 km, but are generally below 100 km. Velocity errors also vary, and show an average of 1.1 m/s. Initial guess trajectories in the Earth-Moon system are significantly less feasible. With the exception of transfer 16, initial guesses feature either a large position error or a large velocity error, or both. Position errors can be as large as 6946 km, and velocity errors can be as large as 80 m/s. These errors are an order of magnitude larger than those for the Sun-Earth system in dimensional units, but due to scale difference between the Sun-Earth and Earth-Moon systems they can be up to four orders of magnitude larger in non-dimensional units.

Table 3 Genetic algorithm initial guess results for the Sun-Earth system.

#	Departure	Arrival	TOF	Δr		Δv		α_{arr}	α_{dep}
1	SE-L1A	SE-L2A	163 days	1.394×10^{-7}	20.87 km	8.669×10^{-6}	0.259 m/s	8.81°	31.46°
2	SE-L1A	SE-L1B	133 days	5.852×10^{-6}	876.1 km	5.970×10^{-6}	0.178 m/s	11.63°	−24.43°
3	SE-L1A	SE-L2B	105 days	5.746×10^{-7}	86.02 km	2.057×10^{-6}	0.061 m/s	23.44°	33.16°
4	SE-L1B	SE-L1A	109 days	7.293×10^{-7}	109.2 km	4.272×10^{-5}	1.277 m/s	33.02°	−18.61°
5	SE-L1B	SE-L2A	156 days	5.545×10^{-9}	0.830 km	4.484×10^{-5}	1.329 m/s	28.65°	57.37°
6	SE-L1B	SE-L2B	151 days	9.858×10^{-7}	147.6 km	7.439×10^{-6}	0.222 m/s	23.04°	−68.90°
7	SE-L2A	SE-L1A	153 days	9.936×10^{-8}	14.87 km	1.331×10^{-4}	3.976 m/s	−44.37°	−11.81°
8	SE-L2A	SE-L1B	179 days	4.475×10^{-8}	6.700 km	5.194×10^{-6}	0.155 m/s	−42.14°	−27.15°
9	SE-L2A	SE-L2B	79 days	6.120×10^{-10}	0.091 km	1.338×10^{-7}	0.004 m/s	−11.72°	−1.44°
10	SE-L2B	SE-L1A	107 days	3.393×10^{-7}	50.79 km	3.186×10^{-7}	0.010 m/s	−44.06°	−16.98°
11	SE-L2B	SE-L1B	194 days	8.637×10^{-8}	12.93 km	1.728×10^{-4}	5.165 m/s	−14.50°	−28.02°
12	SE-L2B	SE-L2A	85 days	4.558×10^{-7}	68.23 km	3.005×10^{-5}	0.898 m/s	−38.83°	12.28°

Table 4 Genetic algorithm initial guess results for the Earth-Moon system.

#	Departure	Arrival	TOF	Δr		Δv		α_{dep}	α_{arr}
13	EM-L1A	EM-L2A	12.6 days	1.807×10^{-2}	6946 km	1.878×10^{-5}	0.019 m/s	−21.50°	−35.56°
14	EM-L1A	EM-L2B	19.2 days	8.711×10^{-9}	0.003 km	6.602×10^{-2}	67.16 m/s	−4.95°	−36.70°
15	EM-L1B	EM-L2A	19.1 days	9.635×10^{-7}	0.370 km	7.682×10^{-2}	78.15 m/s	32.19°	1.58°
16	EM-L1B	EM-L2B	16.6 days	7.191×10^{-7}	0.276 km	1.757×10^{-3}	1.787 m/s	−31.00°	57.23°
17	EM-L2A	EM-L1A	14.8 days	3.273×10^{-7}	0.126 km	7.447×10^{-2}	75.76 m/s	−28.93°	−32.68°
18	EM-L2A	EM-L1B	17.3 days	6.318×10^{-3}	2429 km	7.874×10^{-2}	80.10 m/s	1.84°	−45.74°
19	EM-L2B	EM-L1A	18.6 days	7.377×10^{-3}	2836 km	2.964×10^{-7}	0.000 m/s	39.00°	6.50°
20	EM-L2B	EM-L1B	17.4 days	6.618×10^{-3}	2544 km	7.032×10^{-5}	0.072 m/s	−36.55°	38.21°

V. Results

This section presents the results of the trajectory optimization. Transfers in the Sun-Earth system are discussed in section V.A, and transfers in the Earth-Moon system are presented in section V.B.

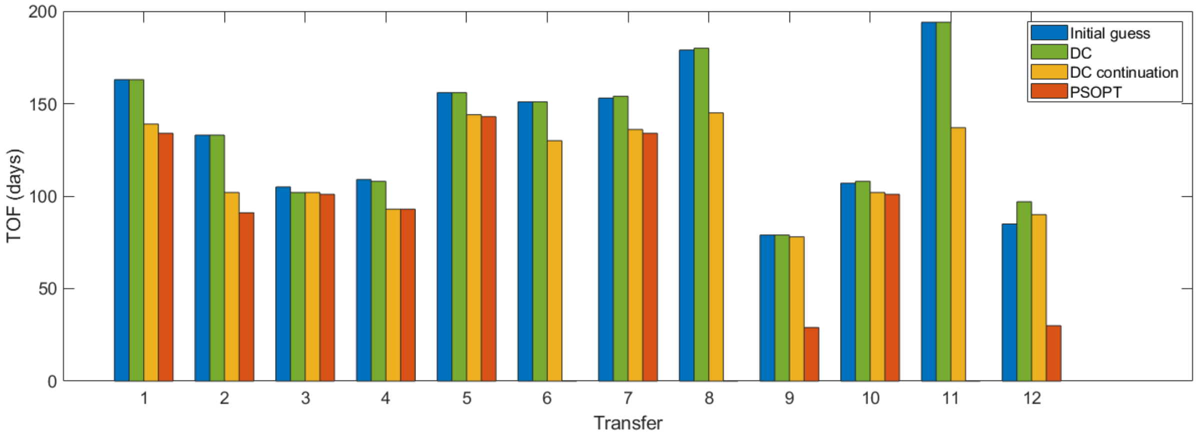

Fig. 7 Transfer times of initial guess and optimized trajectories for the Sun-Earth system.

A. Sun-Earth System Trajectories

Transfer times for the Sun-Earth trajectories are listed in Table 5, and displayed in Fig. 7. Transfer times are reported for the initial (infeasible) guess, the first iteration of the differential corrector (DC), the result of the differential corrector used in continuation on the time of flight, and PSOPT. For most cases, both the differential corrector (after continuation) and PSOPT provide trajectories with substantially shorter flight times compared to the initial guess. PSOPT did not converge on a solution for transfers 6, 8 and 10, whereas the differential corrector converged in all cases. For those cases where PSOPT did converge, it always obtained a shorter time of flight than the differential corrector. In most cases, the difference in flight time was small, but for transfers 9 and 12 the flight time of the PSOPT trajectory was roughly a third of that of the differential corrector. Three transfer cases will be described in detail in this section: transfer 1, where the differential corrector and PSOPT arrive at similar results, transfer 2, where PSOPT obtains a slightly shorter flight time with a distinctly different trajectory, and transfer 9, where PSOPT significantly outperforms the differential corrector.

The trajectories and control profiles for transfer 1, between SE-L1A and SE-L2A, are displayed in Fig. 8. The differential corrector and PSOPT converge on slightly different solutions, both of the same general shape as the initial guess. The PSOPT trajectory both departs and arrives at earlier points along the orbits, and with a flight time of 134 days is slightly faster than the differential corrector trajectory which has a flight time of 139 days. Note that, in the control profiles in Fig. 8 (right), there is a subtle difference in how the initial guess is represented for the differential corrector and PSOPT. Because the differential corrector works with piece-wise constant controls, the cone angle instantaneously jumps from the departure segment value to the arrival segment value. In contrast, PSOPT interpolates the control between the nodes

Table 5 **Transfer times of the initial guess and optimized trajectories in the Sun-Earth system.**

Transfer	Departure	Arrival	Initial Guess	DC Iteration 1	DC Continuation	PSOPT
1	SE-L1A	SE-L2A	163 days	163 days	139 days	134 days
2	SE-L1A	SE-L1B	133 days	133 days	102 days	91 days
3	SE-L1A	SE-L2B	105 days	102 days	102 days	101 days
4	SE-L1B	SE-L1A	109 days	108 days	93 days	93 days
5	SE-L1B	SE-L2A	156 days	156 days	144 days	143 days
6	SE-L1B	SE-L2B	151 days	151 days	130 days	-
7	SE-L2A	SE-L1A	153 days	154 days	136 days	134 days
8	SE-L2A	SE-L1B	179 days	180 days	145 days	-
9	SE-L2A	SE-L2B	79 days	79 days	78 days	29 days
10	SE-L2B	SE-L1A	107 days	108 days	102 days	101 days
11	SE-L2B	SE-L1B	194 days	194 days	137 days	-
12	SE-L2B	SE-L2A	85 days	97 days	90 days	30 days

with Legendre polynomials, which is represented with a linear segment between the arrival and departure values. This convention is also adopted in subsequent figures.

The trajectories and control profiles for transfer 2, between SE-L1A and SE-L1B, are depicted in Fig. 9 and provide an example of a case where PSOPT and the differential corrector converge on distinctly different solutions. The differential corrector obtained a trajectory with a flight time of 102 days, which is 31 days shorter than the initial guess trajectory obtained by the genetic algorithm. PSOPT has converged on a solution that is substantially different from the initial guess, with a flight time of 91 days. This is an illustration of the limitations of using the differential corrector in a continuation process. The method is based on small incremental changes to the initial guess trajectory. Therefore, in order to find a given solution, a continuous path must exist between the initial guess and the solution where each incremental step towards the solution is slightly more optimal than the last. If a better solution exists beyond a region of less optimal trajectories, the differential corrector will not find it. While PSOPT and other optimization techniques are certainly not immune to the problem of converging to local minima, the differential corrector is especially susceptible to it.

Finally, the differential corrector is substantially outperformed by PSOPT for transfers 9 and 12, which are transfers between the same orbit pair, but in opposite direction. Transfer 9 is displayed in Fig. 10. The differential corrector has obtained a trajectory and control profile that is almost unchanged from the initial guess. The final transfer time obtained by the continuation process is 78 days, corresponding to a gain of only one day over the initial guess. The trajectory found by PSOPT is significantly faster, with a transfer time of only 29 days. This is another case where the differential corrector is unable to break out of a local minimum. However, unlike the results for transfer 2, here the local minimum trajectory has a significantly longer transfer time than the trajectory that was found with PSOPT.

Summarizing the results of the Sun-Earth system trajectories, it is clear that PSOPT outperforms the differential corrector

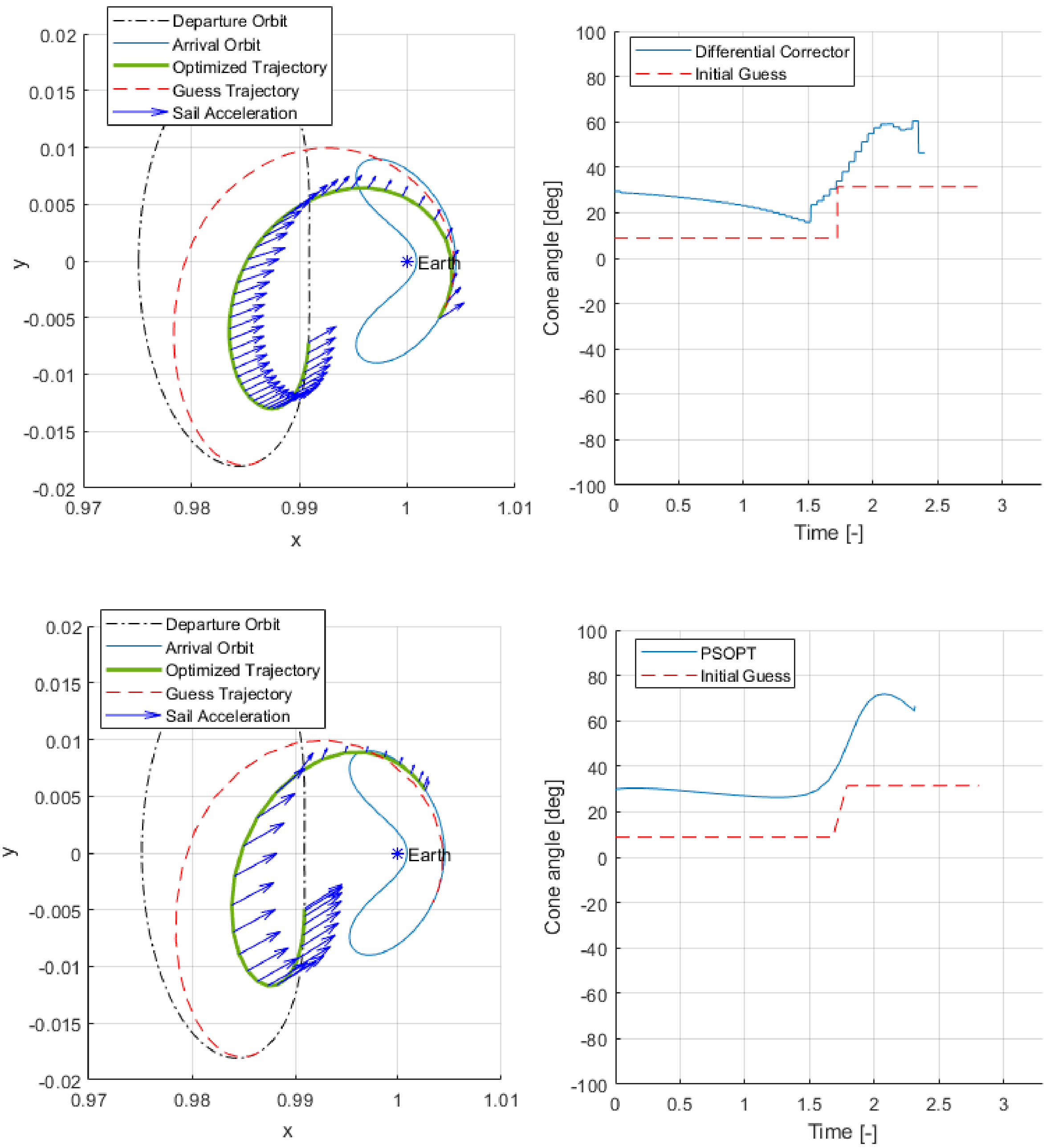

Fig. 8 Optimized trajectory (left) and control over time (right) for transfer 1 (SE-L1A - SE-L2A) using the differential corrector (top) and PSOPT (bottom).

for every trajectory where it converges, in certain cases by a large margin. Furthermore, PSOPT provides a smooth continuous control profile, which is more desirable from a practical perspective, compared to the stepped controls of the differential corrector.

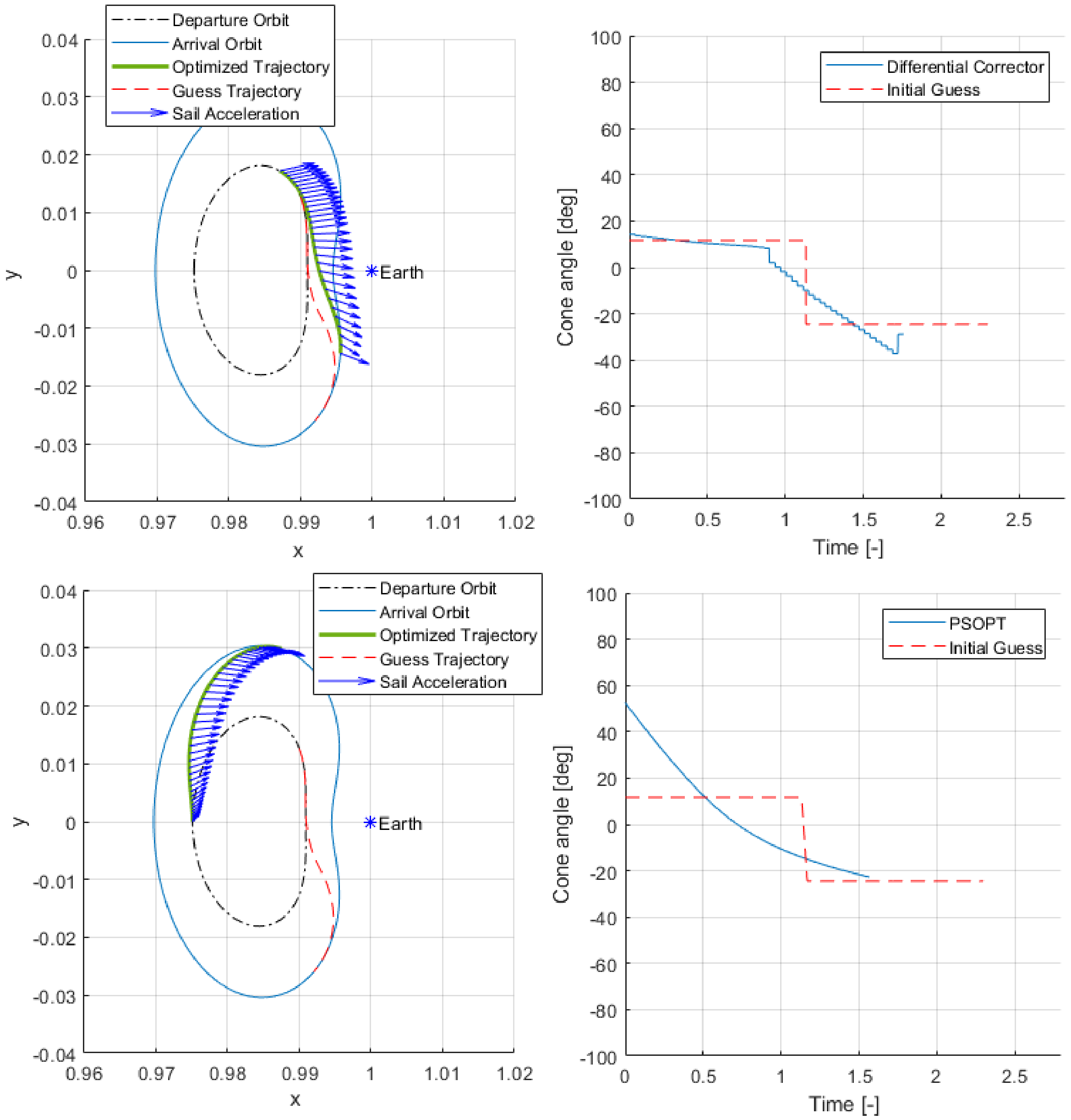

Fig. 9 Optimized trajectory (left) and control over time (right) for transfer 2 (SE-L1A - SE-L1B) using the differential corrector (top) and PSOPT (bottom).

B. Earth-Moon System Trajectories

In contrast to the results for the Sun-Earth system, where PSOPT clearly outperformed differential correction, PSOPT did not yield usable results for the Earth-Moon system trajectories. While PSOPT did converge on a solution for most cases, the control profile associated with these trajectories is not considered feasible for practical purposes. As an example, Fig. 11 displays the control output of the differential corrector and that of PSOPT for transfer 19 (see Table 4), using three different node spacings within PSOPT. The control history provided by PSOPT displays abrupt

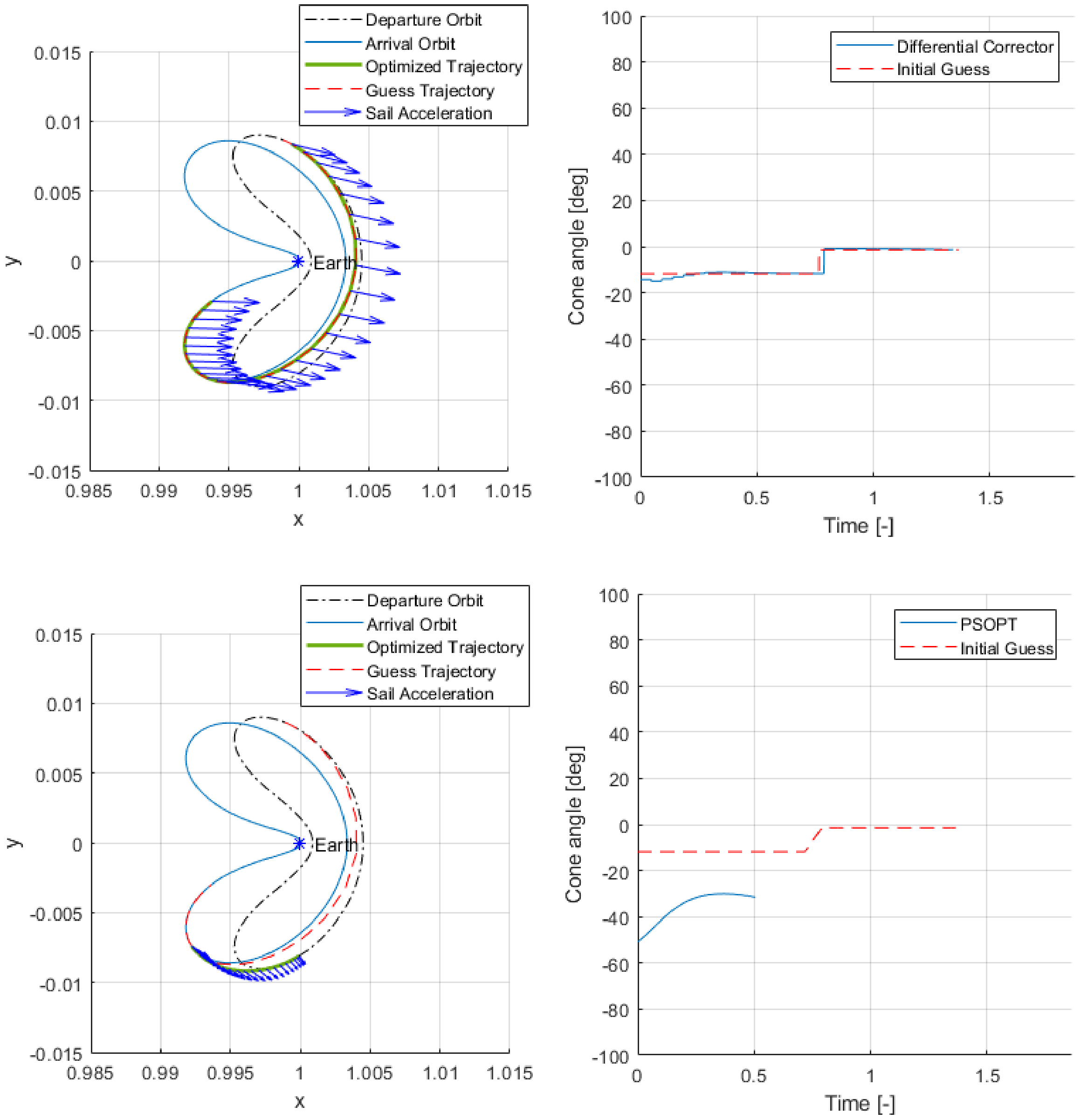

Fig. 10 Optimized trajectory (left) and control over time (right) for transfer 9 (SE-L2A - SE-L2B) using the differential corrector (top) and PSOPT (bottom).

discontinuities, with the cone angle jumping to plus or minus 90 degrees for one or two nodes. Furthermore, many sections display a sawtooth-like pattern around a mean trend line rather than a smooth continuous curve. When constraints are imposed on the cone angle or the control derivative, the method fails to converge at all. These results are typical for all the Earth-Moon system transfers considered in this work. As can be seen in Fig. 11, these effects are reduced when the number of nodes is increased, but are not resolved completely. The fact that the control profile improves so dramatically when the number of nodes is increased indicates that PSOPT is not able to properly handle the time-dependent system dynamics, and in particular the time-dependent nature of the controls, due to the apparent motion of the Sun around the system. When the number of nodes is increased, the change in the direction of the Sun-line over a single trajectory segment is reduced, and the resulting control profile is smoother and more continuous. However, further increasing the number of nodes beyond 100 does not always yield further improvement, and becomes increasingly computationally demanding. When the number of nodes is increased beyond 200, more system memory is required than the 32-bit implementation of PSOPT can address, which imposes a limit on the quality of the obtained results.

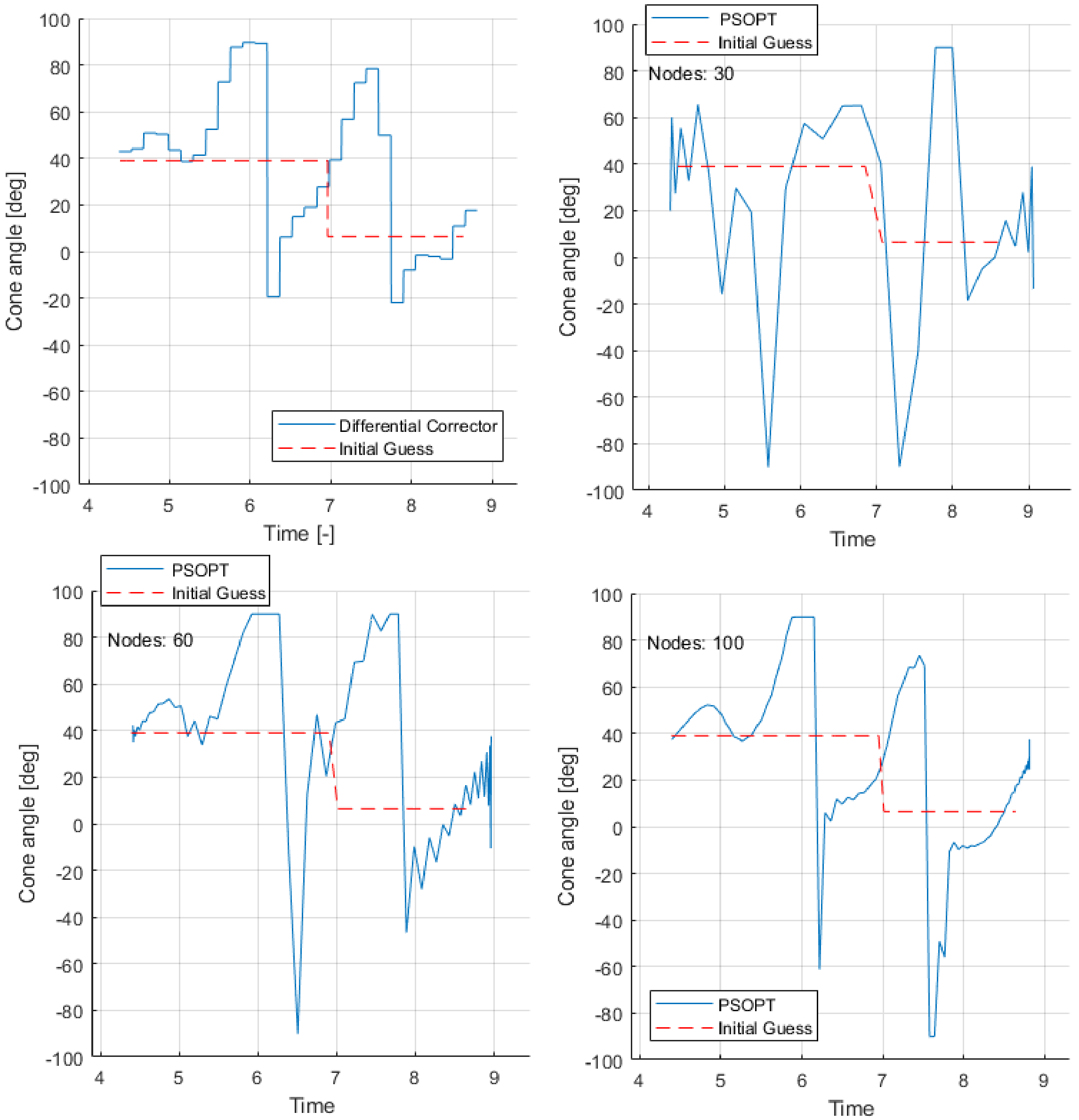

Fig. 11 **Control output for transfer 19 (EM-L2B - EM-L1A) using the differential corrector (top left) and PSOPT with varying node spacing.**

Again, while PSOPT did converge for the Earth-Moon trajectories considered here, the results are considered not practically feasible. To illustrate this, trajectories can be reintegrated outside of PSOPT from the starting condition, with the cone angle at any time interpolated from the PSOPT control output at the nodes using cubic polynomials. Figure 12 compares such reintegrated trajectories for transfers 7 (in the Sun-Earth system) and 19 (in the Earth-Moon system). As can be seen in Fig. 12, the Earth-Moon trajectory eventually diverges from the PSOPT output and terminates far from the target orbit, whereas the reintegrated trajectory matches the PSOPT output for the Sun-Earth system transfer. This can be explained by the fact that PSOPT provides a control output at the nodes, but approximates the controls between the nodes with a series of Legendre polynomials. When the control output is a smooth continuous curve, a simple cubic interpolation allows the trajectory to be accurately reconstructed. However, for the erratic control output obtained for the Earth-Moon system transfers, the complete specification of Legendre polynomials with their respective weighting factors would have to be provided in order to reconstruct the trajectory outside of PSOPT. This greatly limits the usefulness of the PSOPT results, and consequently only the results of the differential corrector are reported for the Earth-Moon system transfers.

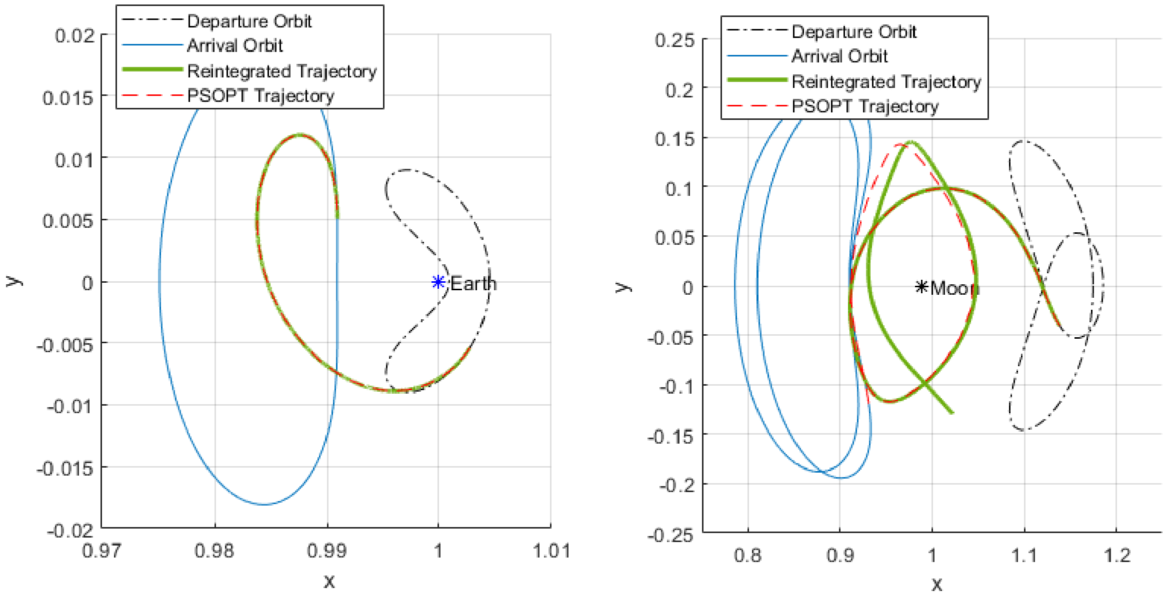

Fig. 12 Reintegrated trajectory compared to PSOPT output for transfers 7 (in the Sun-Earth system, left) and 19 (in the Earth-Moon system, right).

Transfer times for the Earth-Moon system trajectories are listed in Table 6 and displayed in Fig. 13. As mentioned, PSOPT did not yield easily reproducible results for the Earth-Moon system transfers. The differential corrector also failed to converge for transfers 13 and 17, between the EM-L1A and EM-L2A orbits. For the remaining six cases, the final transfer times obtained from the differential corrector (after continuation) are shorter than the initial guess in only two cases. This can be explained as a consequence of the relative infeasibility of the initial guesses produced by the genetic algorithm, which in most cases exhibited large discontinuities in either position or velocity. As a result, the differential corrector initially (i.e., before continuation) converged to trajectories with longer flight times than the initial guess.

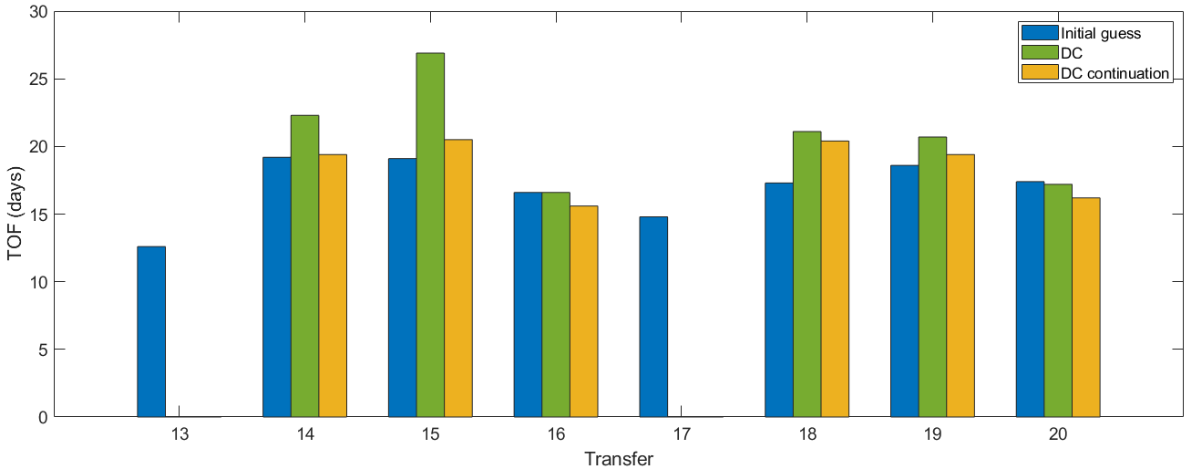

Fig. 13 Transfer times of initial guess and optimized trajectories for the Earth-Moon system.

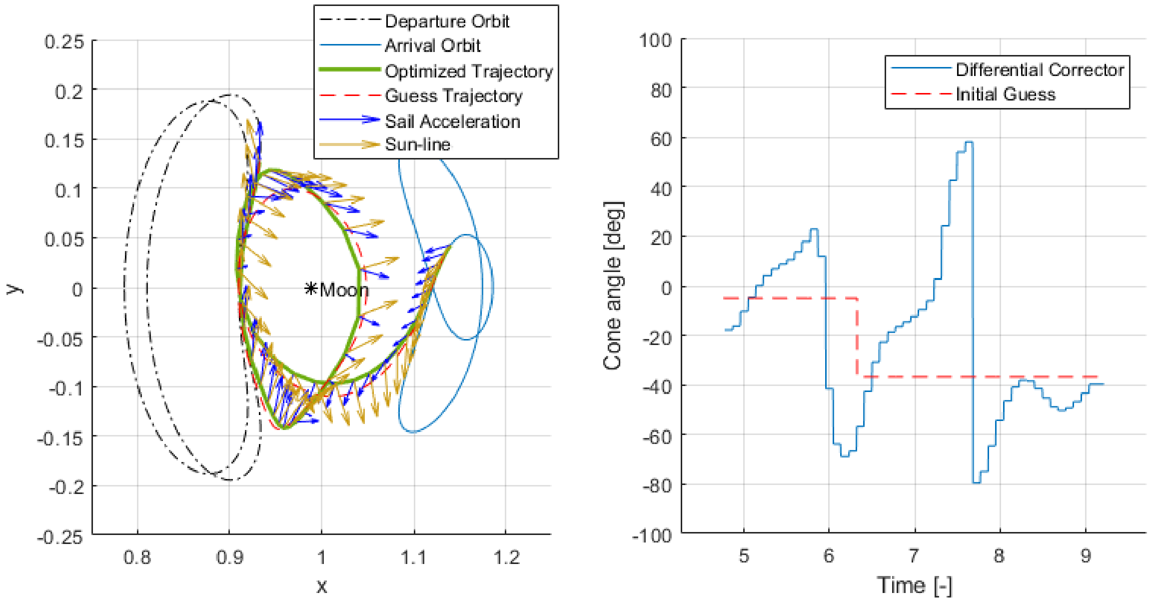

Fig. 14 Optimized trajectory (left) and control over time (right) for the EM-L1A - EM-L2B (14) transfer using the differential corrector.

Optimized trajectories and control histories are given in Fig. 14 for transefer 14 (EM-L1A - EM-L2B) and in Fig. 15 for transfer 16 (EM-L1B - EM-L2B). Both trajectories closely resemble their initial guess. The differential corrector obtained transfer times of 19.4 and 15.6 days, compared to initial guess transfer times of 19.2 and 16.6 days, respectively. Obtaining feasible trajectories resulted in control histories that display a sinusoidal pattern, which is typical for all transfers in the Earth-Moon system, and could also be seen in the control output of PSOPT displayed in Fig. 11. Another feature of the control histories is the presence of large discontinuous changes in the sail attitude of 140 degrees or more, which were not seen in the Sun-Earth system transfers. The need for these changes is another effect of the time-varying direction of the incoming solar radiation, and are likely to be problematic in practice.

Table 6 Transfer times of the initial guess and optimized trajectories in the Earth-Moon system.

Transfer	Departure	Arrival	Initial Guess	DC Iteration 1	DC Continuation	PSOPT
13	EM-L1A	EM-L2A	12.6 days	-	-	-
14	EM-L1A	EM-L2B	19.2 days	22.3 days	19.4 days	-
15	EM-L1B	EM-L2A	19.1 days	26.9 days	20.5 days	-
16	EM-L1B	EM-L2B	16.6 days	16.6 days	15.6 days	-
17	EM-L2A	EM-L1A	14.8 days	-	-	-
18	EM-L2A	EM-L1B	17.3 days	21.1 days	20.4 days	-
19	EM-L2B	EM-L1A	18.6 days	20.7 days	19.4 days	-
20	EM-L2B	EM-L1B	17.4 days	17.2 days	16.2 days	-

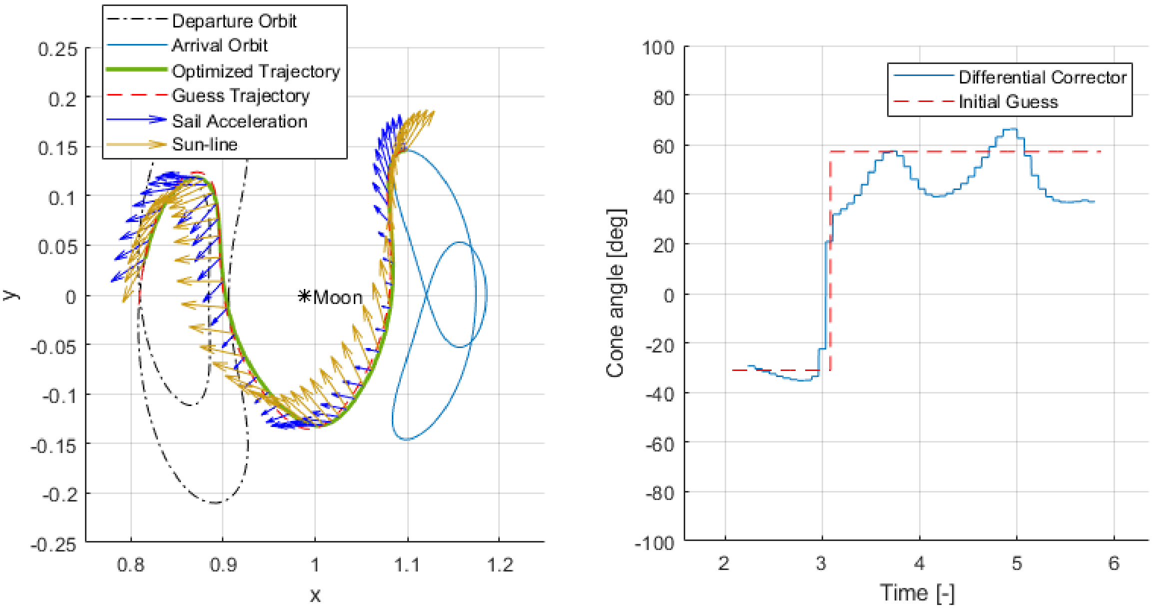

Fig. 15 Optimized trajectory (left) and control over time (right) for the EM-L1B - EM-L2B (16) transfer using the differential corrector.

VI. Conclusion

This paper has found time-optimal transfer trajectories between solar-sail displaced libration point orbits around the L_1 and L_2 points of the Sun-Earth and Earth-Moon systems. Initial guess trajectories based on a two-phase transfer, with piece-wise constant sail attitudes and state errors between the two phases, were obtained using a genetic-algorithm approach. These trajectories were then made feasible and their time of flight was optimized using multiple shooting with differential correction and pseudospectral collocation as implemented by the open-source software package PSOPT. The performance of these two methods was subsequently compared.

For transfers in the Sun-Earth system, PSOPT generally outperforms differential correction, yielding trajectories with flight times as short as 29 days for transfers between L_2-point orbits, and as short as 101 days for transfers between L_1 and L_2-point orbits. Multiple shooting with differential correction obtained transfer trajectories with transfer times that were only slightly longer than those obtained by PSOPT for most cases, with transfer times between L_1 and L_2-point orbits as short as 102 days. However, in certain transfer cases, the PSOPT trajectory is shorter by as much as 60 days, because the differential corrector is more susceptible to converging to a local minimum. The differential corrector always converged on a solution, whereas PSOPT failed to converge in three out of twelve cases.

For transfers in the Earth-Moon system, PSOPT proved unable to properly handle the time-dependent system dynamics, providing trajectories with control histories that were not reproducible outside PSOPT. The differential corrector converged for six out of eight cases, yielding trajectories with transfer times as short as 15.6 days. From the results obtained in the Sun-Earth system it seems reasonable to expect shorter transfer trajectories can be obtained by a more powerful optimization method, given the limitations of the differential corrector. Because these trajectories are already relatively short however, a more fruitful area for future research might be finding a method to limit the large discontinuities in cone angle that are present in all transfers in the Earth-Moon system, as these are likely to present considerable practical difficulties in an actual mission.

Acknowledgments

The author gratefully acknowledges Alvaro Fernandez Mora and Jeannette Heiligers for providing initial conditions for the periodic orbits used in this work.

References

[1] McInnes, C., *Solar Sailing: Technology, Dynamics and Mission Applications*, Springer-Praxis, Berlin, 1999.

[2] Sawada, H., Mori, O., Okuizumi, N., Shirasawa, Y., Miyazaki, Y., Natori, M., Matunaga, S., Furuya, H., and Sakamoto, H., "Mission Report on The Solar Power Sail Deployment Demonstration of IKAROS," *52nd AIAA Structures, Structural Dynamics and Materials Conference*, Denver, 2011.

[3] Johnson, L., Young, R., Montgomery, E., and Alhorn, D., "Status of Solar Sail Technology Within NASA," *Advances in Space Research*, Vol. 48, 2011, pp. 1687–1694.

[4] Betts, B., Nye, B., Vaughn, J., Greeson, E., Chute, R., Spencer, D., Ridenoure, R., Munakata, R., Wong, S., Diaz, A., Stetson, D., Foley, J., Bellardo, J., and Plante, B., "LightSail 1 Mission Results and Public Outreach Strategies," *Fourth International Symposium on Solar Sailing*, Kyoto, 2017.

[5] Davis, J., "LightSail 2 Spacecraft Successfully Demonstrates Flight by Light," , 2019. URL `https://www.planetary.org/blogs/jason-davis/lightsail-2-successful-flight-by-light.html`, accessed: 24.11.2019.

[6] Verrier, P., Waters, T., and Sieber, J., "Evolution of the L_1 Halo Family in the Radial Solar Sail CRTBP," *Celestial Mechanics and Dynamical Astronomy*, Vol. 120, 2013.

[7] Heiligers, J., Macdonald, M., and Parker, J., "Extension of Earth-Moon Libration Point Orbits with Solar Sail Propulsion," *Astrophysics and Space Science*, Vol. 361 (7), 2016.

[8] Heiligers, J., Parker, J., and Macdonald, M., "Novel Solar Sail Mission Concepts for High-Latitude Earth and Lunar Observation," *Astrodynamics Specialist Conference*, Long Beach, 2016.

[9] Sweetser, T., Broschart, S., Angelopoulos, V., Whiffen, G., Folta, D., Chung, M.-K., Hatch, S., and Woodard, M., "ARTEMIS Mission Design," *Space Science Reviews*, Vol. 165, 2011.

[10] Folta, D., Woodard, M., Sweetser, T., Broschart, S., and Cosgrove, D., "Design and Implementation of the ARTEMIS Lunar Transfer Using Multi-Body Dynamics," 2011, p. 1647.

[11] Sood, R., and Howell, K., "L_4, L_5 Solar Sail Transfers and Trajectory Design: Solar Observations and Potential Earth Trojan Exploration," *26th AAS/AIAA Space Flight Mechanics Meeting*, Napa, 2016.

[12] Farres, A., Heiligers, J., and Miguel, N., "Road Map to L_4/L_5 With a Solar Sail," *Aerospace Science and Technology*, Vol. 95, 2019.

[13] Fernandez, A., Heaton, A., and Heiligers, J., "Solar-sail Transfers From Invariant Objects to L5 Periodic Orbits," *7th International Conference on Astrodynamics Tools and Techniques*, Oberpfaffenhofen, 2018.

[14] Van Den Oever, T., and Heiligers, J., "On the Design of Transfers to Solar-Sail Displaced Orbits in the Earth-Moon System," *7th International Conference on Astrodynamics Tools and Techniques*, Oberpfaffenhofen, 2018.

[15] Heiligers, J., "Homo- and Heteroclinic Connections in the Planar Solar-Sail Earth-Moon Three-Body Problem," *Frontiers in applied mathematics and statistics*, Vol. 3, 2018.

[16] Becerra, V., "Solving Complex Optimal Control Problems at No Cost with PSOPT," *2010 IEEE International Symposium on Computer-Aided Control System Design*, Yokohama, 2010.

[17] Wakker, K., *Fundamentals of Astrodynamics*, TU Delft Institutional Repository, Delft, 2015.

[18] Rios-Reyes, L., and Scheeres, D., "Solar-Sail Navigation: Estimation of Force, Moments, and Optical Parameters," *Journal of Guidance, Control and Dynamics*, Vol. 30 (3), 2007, pp. 660–668.

[19] Dachwald, B., and Macdonald, M., "Parametric Model and Optimal Control of Solar Sails with Optical Degradation," *Journal of Guidance, Control and Dynamics*, Vol. 29 (5), 2006, pp. 1170–1178.

[20] Mingotti, G., Heiligers, J., and McInnes, C., "Optimisation of Solar Sail Interplanetary Heteroclinic Connections," *2nd Conference on Dynamics and Control of Space Systems*, Rome, 2014.

[21] Heiligers, J., Fernandez, J., Stohlman, O., and Wilkie, W., "Trajectory Design for a Solar-Sail Mission to Asteroid 2016 HO3," *Astrodynamics*, Vol. 3, 2019, pp. 231–246.

[22] Kirk, D., *Optimal Control Theory - An Introduction*, Prentice-Hall, Englewood Cliffs, New Jersey, 1970.

[23] Koon, W. S., Lo, M., Marsden, J., and Ross, S., *Dynamical Systems, the Three-body Problem and Space Mission Design*, Springer-Verlag, New York, 2007.

[24] Farquhar, R., and Kamel, A., "Quasi-Periodic Orbits About the Translunar Libration Point," *Celestial Mechanics*, Vol. 7, 1973, pp. 458–473.

[25] Wächter, A., and Biegler, L., "On the Implementation of a Primal-Dual Interior Point Filter Line Search Algorithm for Large-Scale Nonlinear Programming," *Mathematical Programming*, Vol. 106, 2006, pp. 25–57.

[26] Becerra, V., "PSOPT Optimal Control Solver User Manual," Tech. rep., Available online at https://github.com/PSOPT/psopt/blob/master/PSOPT/doc/PSOPT_Manual_R4.pdf, 2019. Accessed: 2019-11-02.

[27] Parker, J., and Anderson, R., *Low-energy Lunar Trajectory Design*, Wiley, Hoboken, New Jersey, 2014.

3

Conclusions and Recommendations

This chapter contains the conclusions that can be drawn from the thesis work which was presented in chapter 2. Section 3.1 presents answers to the research questions, and section 3.2 provides recommendations for future work.

3.1. Conclusions

The objective of this thesis was to add to the literature by finding time-optimal transfer trajectories between a number of solar-sail displaced libration point orbits around the L_1 and L_2 points of the Sun-Earth and Earth-Moon systems. Two methods for finding these trajectories were compared: direct pseudospectral collocation, as implemented in the open-source software package PSOPT (Becerra, 2010), and multiple shooting with differential correction. This section provides a summary of the main findings by answering the research questions that were introduced in section 1.2.

I. What are the time-optimal transfer trajectories between solar-sail displaced orbits around the colinear libration points of the the Sun-Earth and Earth-Moon systems?

Time-optimal transfer trajectories were found in the Sun-Earth and Earth-Moon systems. In the Sun-Earth system, trajectories were obtained with transfer times as short as 91 days for transfers between L_1 and L_2 orbits, and as short as 29 days for transfers between orbits around the same libration point. These transfer trajectories are up to 64% faster than the two-segment initial guess trajectories, which were obtained with simple fixed controls in each segment. In the Earth-Moon system, trajectories were found with transfer times as short as 15.6 days for transfers between L_1 and L_2 orbits. In contrast to the results in the Sun-Earth system, the improvement in flight time compared to the initial guess is modest. In the best case, the reduction in flight time was limited to 7%.

II. How do transfer trajectories in the Sun-Earth system differ from those in the Earth-Moon system?

Initial guess trajectories in the Earth-Moon system were significantly less feasible than those found for the Sun-Earth system. In non-dimensional units, the magnitude of the position and velocity discontinuities between the departure and arrival trajectory segments was up to four orders of magnitude larger in the Earth-Moon system than in the Sun-Earth system. These large discontinuities in the initial guess trajectories proved to be challenging for the differential corrector, which initially converged to transfer trajectories with significantly longer flight times than the initial guess. Consequently, the flight times of the trajectories after continuation on the time of flight show only modest improvement over the initial guess.

Control profiles for transfers in the Sun-Earth system are smooth and continuous, with maximum absolute cone angles of roughly 70°. The control profiles for transfers in the Earth-Moon system show a sinusoidal pattern in the cone angle over time, along with large discontinuous jumps of up to 140 degrees. These features are a consequence of the time-dependency of the system, introduced by the apparent rotation of the Sun. The large discontinuous jumps are likely to present significant difficulties in practice.

III. Which optimization method is most suitable to find time-optimal transfer trajectories between solar-sail displaced libration point orbits in the Sun-Earth and Earth-Moon systems?

For transfers in the Sun-Earth system, PSOPT generally outperforms the differential correction method. For all transfers where PSOPT converges on a solution, the obtained transfer time is shorter than the one obtained by the differential corrector. The difference in transfer times between the two methods is usually small, but in some cases where the differential corrector gets stuck in a local minimum, the PSOPT trajectory can be faster by as much as a factor of three. While PSOPT failed to converge on a solution in three cases, the differential corrector always converged. In total, out of the twelve transfers that were investigated, PSOPT produced slightly faster trajectories in seven cases, significantly faster trajectories in two cases, and failed to converge in three cases. In addition to providing faster trajectories, the control profiles produced by PSOPT are continuous, while those provided by the differential corrector are step-wise constant. Because it produces faster trajectories with more desirable control profiles, it can be concluded that PSOPT is the more suitable method for finding transfers in the Sun-Earth system.

For transfers in the Earth-Moon system, PSOPT failed to provide feasible trajectories by either not converging on a solution, or by converging on solutions with erratic control profiles which could not be reproduced outside of PSOPT. The differential corrector did converge on a solution in six out of eight cases, but the trajectories that were found feature discontinuities in the control profile, which may be difficult to achieve in practice. Because PSOPT failed to provide any feasible trajectories, the differential corrector is the most suitable method for transfers in the Earth-Moon system, but further work is required to obtain trajectories with practically feasible controls.

3.2. Recommendations

This work has presented time-optimal transfer trajectories between planar Lyapunov orbits around the L_1 and L_2 points of the Sun-Earth and Earth-Moon systems. This section provides some suggestions for future research.

Employ dynamic node spacing
In order to minimize the Runge phenomenon, Legendre-Gauss-Lobatto (LGL) node spacing or a similar scheme is required by PSOPT. The transfers between L_1 and L_2 orbits studied in this work usually feature a flyby of the smaller primary body. The system dynamics are highly non-linear at close approaches. These approaches by necessity occur roughly halfway in the trajectory, which is where the LGL node spacing is extremely sparse. Increasing the total number of nodes becomes computationally infeasible beyond 150 nodes because of memory limitations. A collocation method which makes use of dynamic node spacing, and can thus offer more densely spaced nodes in these highly non-linear regions, may produce better results.

Employ a multi-phase approach
Another solution to the node spacing problem discussed in the previous paragraph may be to employ a multi-phase approach, where the trajectory is divided into a departure, flyby, and arrival phase. By properly choosing the relative lengths of these phases, PSOPT may be able to more properly account for the highly non-linear dynamics while retaining the LGL node spacing. The convergence of the differential corrector may also benefit from a multi-phase approach, by generating step updates for the highly non-linear flyby phase separately from the comparatively more stable departure and arrival phases.

Use a 64-bit implementation of PSOPT
Results in the Earth-Moon system show that the trajectories PSOPT provides become more feasible when the number of nodes is increased, as the increased node density mitigates the problem introduced by the time-dependency of the system. The number of nodes that can be used is strictly limited by the amount of system memory that can be addressed by the 32-bit implementation of PSOPT that

was used in this paper. By making use of a 64-bit compiler it will be possible to increase the number of nodes, although at the cost of greatly increasing the computation time.

Use interpolated controls in the differential corrector

The differential corrector as specified in this work uses step-wise continuous controls between the nodes. This can lead to large discontinuities in the cone angle from one node to the next, which may not be feasible in practice. These discontinuities in cone angle can be eliminated by using interpolated controls between the nodes. Linear interpolation would be relatively straightforward to implement, by making the cone angle a function of the cone angle at adjacent nodes and time and adding the appropriate partial derivatives to the state transition matrices. The resulting control profile may still require rapid changes in the cone angle at the nodes. More elaborate interpolation schemes can provide a smoother control profile, but this would require modifying the method to allow for constraints that act on more than the immediately adjacent nodes.

Investigate the time-dependency of the Earth-Moon system

Both PSOPT and the differential corrector obtained better results in the Sun-Earth system. There are two main differences between the Sun-Earth and the Earth-Moon systems. The first is the time-dependency introduced by the non-stationary Sun in the Earth-Moon system. The second is a scale difference caused by the difference in the mass ratio between the Sun and the Earth and the Earth and the Moon. The latter effect may be responsible for part of the difference in performance between the two systems, as the ratio between solar-sail acceleration and gravitational acceleration by the smaller primary body during close approaches differs substantially. To disentangle these effects, transfers could be investigated for a fictitious autonomous system with the Sun as the larger primary body, but with the mass ratio of the Earth-Moon system, or with several intermediary mass ratios.

Investigate three-dimensional orbits

The departure and arrival orbits used for the transfers studied in this work were planar Lyapunov orbits. Because the Sun was assumed to be in the same plane as the orbits, the resulting trajectories are two-dimensional. Three-dimensional displaced libration point orbits have also been found (Heiligers et al., 2016). The methods used in this work can be readily adapted to find transfer trajectories between these orbits as well. By adding a sail clock angle (McInnes, 1999) as an additional control variable, three-dimensional trajectories can be obtained using the same methodology that was used in this paper.

Use a more realistic solar-sail force model

The orbits and transfer trajectories studied in this work used a solar-sail force model based on perfect reflection. For such a model, the sail acceleration is directed along the sail normal vector. A higher fidelity model which incorporates diffuse reflection and absorption would add an acceleration component that is tangential to the sail normal vector (Forward, 1989), and provide more realistic results.

Use higher fidelity system dynamics

The work in this paper made use of the circular restricted three-body model, which is an idealization of the true system dynamics. Properly accounting for the elliptical orbits of the Earth and Moon, and in the case of the Earth-Moon system, the inclination between the Earth-Moon orbital plane and the plane of the ecliptic, will provide more realistic trajectories.

A

Verification and validation

This appendix contains the verification and validation of the primary methods that have been used to obtain the results in this work.

A.1. Three-body dynamics

The circular restricted three-body dynamics can be verified by examining the accelerations produced by the model for an object placed at one of the classic libration points with zero velocity. If correctly implemented, these accelerations should be zero. An orthogonal xyz reference frame was defined in Section II of Chapter 2. Within this reference frame, the x-coordinates of the three co-linear libration points can be found by solving (Wakker, 2015):

$$x - (1-\mu)\frac{\mu + x}{|\mu + x|^3} + \mu\frac{1-\mu-x}{|1-\mu-x|^3} = 0. \tag{A.1}$$

The three real roots of Eq. A.1 can be found by the *fzero.m* routine in MATLAB®. These x-coordinates are then used to construct state vectors for stationary objects in the libration points, by setting all other variables to zero. Table A.1 displays these state vectors, as well as the resulting accelerations produced by the three-body dynamics model. As can be seen in Table A.1, these accelerations are negligible, and the correct implementation of the three-body system is verified.

Table A.1: Earth-Moon system model accelerations at the three co-linear libration points.

Libration point	State vector	$\ddot{x}$	$\ddot{y}$
L_1	[0.836918; 0; 0; 0]	2.220×10^{-16}	0
L_2	[1.155680; 0; 0; 0]	-6.661×10^{-16}	0
L_3	[-1.005062; 0; 0; 0]	-4.441×10^{-16}	0

A.2. Solar-sail acceleration

For a perfectly reflecting sail, the solar-sail acceleration is directed along the sail normal vector. The magnitude of the sail acceleration depends on the cone angle between the sail normal vector and the Sun-line. As the cone angle increases, the acceleration provided by the sail decreases due to a decrease in the projected surface area of the sail facing the Sun. The normalized sail acceleration obtained from the solar-sail force model is displayed in the left panel of Fig. A.1. The normalized sail acceleration given by McInnes (1999) is displayed in the right panel for comparison. As can be seen in Fig A.1, the acceleration from the sail force model matches the acceleration found in the reference.

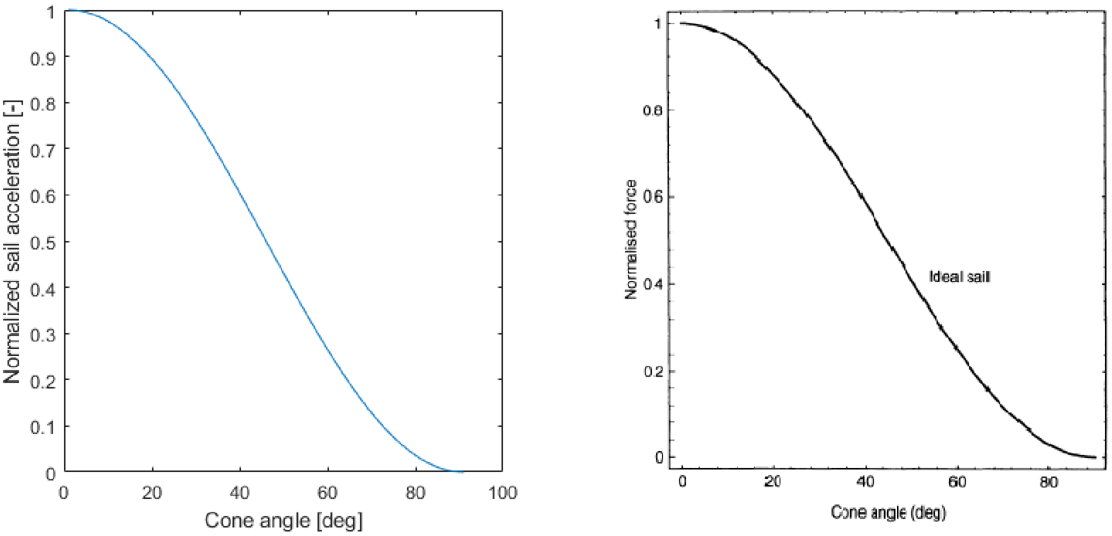

Figure A.1: Normalized sail acceleration as a function of cone angle obtained from force model (left) and McInnes (1999) (right).

A.3. Trajectory propagation

Trajectories are propagated by means of the *ode45.m* routine in MATLAB®. The arrival and departure orbits for the transfer trajectories studied in this work provide a convenient way to verify the accuracy of the numerical integration, as well as the three-body dynamics and solar-sail force model. After propagating a solar-sail enabled orbit for one period, the final orbit state should be identical to the starting state.

The difference between the starting orbit state and the orbit state after one period of integration is displayed in Table A.2 for two orbits in the Earth-Moon system, and one orbit in the Sun-Earth system. As can be seen in Table A.2, the difference in state variables is negligible for all three orbits. Because these orbits are very unstable, small errors in the three-body dynamics, solar-sail force model, or numerical integration scheme would have produced substantial deviations in the end states of the orbits. Those three factors can therefore be considered to be verified.

Table A.2: Difference in state variables between starting state and state after one period.

Orbit	Steering Law	x	y	$\dot{x}$	$\dot{y}$
EM-L1A	Earth-Moon line	4.155×10^{-10}	2.208×10^{-10}	8.420×10^{-10}	4.577×10^{-10}
EM-L1B	Sun line	2.312×10^{-10}	5.700×10^{-10}	1.936×10^{-9}	8.035×10^{-10}
SE-L1A	Sun line	1.703×10^{-13}	4.446×10^{-13}	6.857×10^{-13}	1.381×10^{-13}

A.4. PSOPT Implementation

To verify the correct implementation of the optimization problem in PSOPT, an optimized trajectory is sought for a homoclinic connection between two points along the SE-L1B orbit. The departure and arrival points along the orbit are fixed. A deliberately poor initial guess is generated by propagating the trajectory from these points with a fixed cone angle of 40 degrees. An integral cost function consisting of the square of the cone angle is used instead of the time of flight. The optimal solution to this problem is known in advance: the trajectory should follow the original orbit, with a constant cone angle of zero.

The optimized trajectory and cone angle over time for the initial guess and the PSOPT output are displayed in Fig. A.2. As can be seen, PSOPT has found the expected solution, despite the initial guess being highly infeasible.

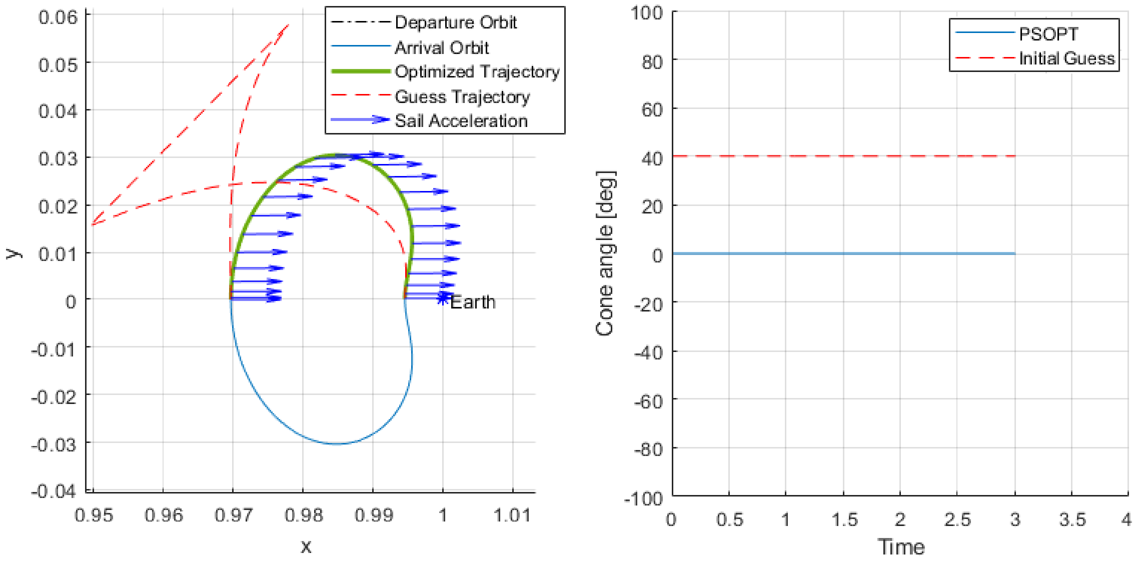

Figure A.2: Trajectory (left) and control output over time (right) for a homoclinic connection for the SE-L1B orbit using PSOPT top optimize for minimum control effort.

A.5. Trajectory validation

To validate the optimized trajectories that are provided by PSOPT and the differential corrector, they can be reintegrated in MATLAB®. For PSOPT trajectories, the cone angle between the nodes is approximated by a quadratic polynomial. For trajectories obtained from the differential corrector, the same step-wise constant controls as used in the differential correction method are applied. The result of the reintegrated PSOPT trajectory for transfer 3 is displayed in Fig. A.3. The reintegrated trajectory is identical to the PSOPT output.

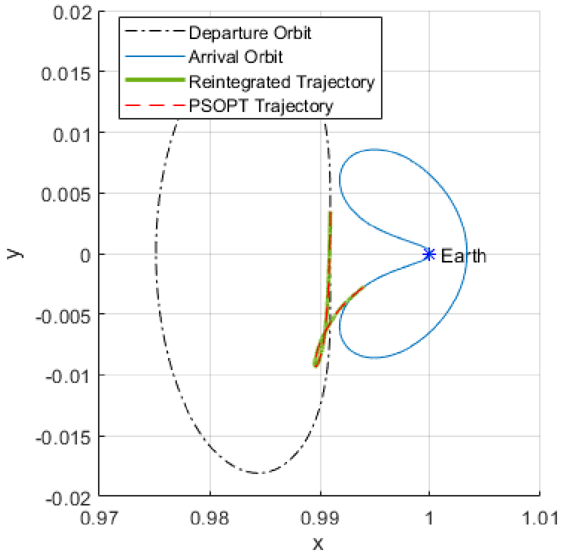

Figure A.3: Comparison of reintegrated trajectory and PSOPT output for transfer 3 (SE-L1A - SE-L2B).

Table A.3 displays the deviations in the state variables for transfer 3 at the end of the reintegrated trajectories, compared to the output of PSOPT and the differential corrector. As can be seen, the deviations are small, and on the order of the 1×10^{-6} convergence tolerances that were set for PSOPT and the level two differential corrector. The deviations slightly exceed the tolerance. For PSOPT, this can be explained by the error introduced by interpolating the controls between the nodes by quadratic polynomials for the reintegration, whereas PSOPT uses Legendre polynomials. In the case of the differential corrector, the deviations are caused by small residual $\Delta\boldsymbol{V}$s at the nodes. These $\Delta\boldsymbol{V}$s are individually below the tolerance, but the errors they introduce compound over the whole trajectory.

Table A.3: Deviation of state variables at the end of the reintegrated trajectories for transfer 3.

Method	Δx	Δy	$\Delta \dot{x}$	$\Delta \dot{y}$
PSOPT	-2.5946×10^{-6}	3.6863×10^{-6}	-2.1939×10^{-7}	-2.3674×10^{-7}
Differential corrector	1.1323×10^{-6}	-2.1326×10^{-7}	3.411×10^{-6}	5.960×10^{-7}

Bibliography

Becerra, V. Solving Complex Optimal Control Problems at No Cost with PSOPT. In *2010 IEEE International Symposium on Computer-Aided Control System Design*, Yokohama, 2010.

Betts, B., Nye, B., Vaughn, J., Greeson, E., Chute, R., Spencer, D., Ridenoure, R., Munakata, R., Wong, S., Diaz, A., Stetson, D., Foley, J., Bellardo, J., and Plante, B. LightSail 1 Mission Results and Public Outreach Strategies. In *Fourth International Symposium on Solar Sailing*, Kyoto, 2017.

Ceriotti, M. and McInnes, C. Natural and Sail-Displaced Doubly-Symmetric Lagrange Point Orbits for Polar Coverage. *Celestial Mechanics and Dynamical Astronomy*, 114:151–180, 2012.

Davis, J. LightSail 2 Spacecraft Successfully Demonstrates Flight by Light, 2019. URL `https://www.planetary.org/blogs/jason-davis/lightsail-2-successful-flight-by-light.html`. accessed: 24.11.2019.

Farres, A., Heiligers, J., and Miguel, N. Road Map to L_4/L_5 with a Solar Sail. *Aerospace Science and Technology*, 95, 2019.

Fernandez, A., Heaton, A., and Heiligers, J. Solar-sail Transfers From Invariant Objects to L_5 Periodic Orbits. In *7th International Conference on Astrodynamics Tools and Techniques*, Oberpfaffenhofen, 2018.

Fimple, W. Generalized Three-Dimensional Trajectory Analysis of Planetary Escape by Solar Sail. *ARS Journal*, 32:883–887, 1962.

Folta, D., Woodard, M., Sweetser, T., Broschart, S., and Cosgrove, D. Design and Implementation of the ARTEMIS Lunar Transfer Using Multi-Body Dynamics. volume 142, page 1647, 08 2011.

Forward, R. Gray Solar Sails. In *25th AIAA Joint Propulsion Conference*, Monterey, 1989.

Friedman, L., Carroll, W., Goldstein, R., Jacobson, R., Kievit, J., Landel, R., Layman, W., Marsh, E., Ploszaj, R., Rowe, W., Ruff, W., Stevens, J., Stimpson, L., Trubert, M., Varsi, G., and Wright, J. Solar Sailing : The Concept Made Realistic. In *16th AIAA Aerospace Sciences Meeting*, Huntsville, 1978.

Garwin, R. Solar Sailing - A Practical Method of Propulsion Within the Solar System. *Jet Propulsion*, 28:188–190, 1958.

Heiligers, J. Homo- and Heteroclinic Connections in the Planar Solar-Sail Earth-Moon Three-Body Problem. *Frontiers in Applied Mathematics and Statistics*, 3, 2018.

Heiligers, J., Macdonald, M., and Parker, J. Extension of Earth-Moon Libration Point Orbits with Solar Sail Propulsion. *Astrophysics and Space Science*, 361 (7), 2016.

Johnson, L., Young, R., Montgomery, E., and Alhorn, D. Status of Solar Sail Technology Within NASA. *Advances in Space Research*, 48:1687–1694, 12 2011.

McInnes, C. *Solar Sailing: Technology, Dynamics and Mission Applications*. Springer-Praxis, Berlin, 1999.

Sands, N. Escape From Planetary Gravitational Fields by Use of Solar Sails. *ARS Journal*, 31:527–531, 1961.

Sawada, H., Mori, O., Okuizumi, N., Shirasawa, Y., Miyazaki, Y., Natori, M., Matunaga, S., Furuya, H., and Sakamoto, H. Mission Report on The Solar Power Sail Deployment Demonstration of IKAROS. In *52nd AIAA Structures, Structural Dynamics and Materials Conference*, Denver, 2011.

Sood, R. and Howell, K. L_4, L_5 Solar Sail Transfers and Trajectory Design: Solar Observations and Potential Earth Trojan Exploration. In *26th AAS/AIAA Space Flight Mechanics Meeting*, Napa, 2016.

Sweetser, T., Broschart, S., Angelopoulos, V., Whiffen, G., Folta, D., Chung, M.-K., Hatch, S., and Woodard, M. ARTEMIS Mission Design. *Space Science Reviews*, 165, 09 2011.

Tsander, F. From a Scientific Heritage, 1924. Translated as NASA technical report NASA-TT-F-541, available online at https://ntrs.nasa.gov/search.jsp?R=19690016734, accessed 2020-03-29.

Tsu, T. Interplanetary Travel by Solar Sail. *ARS Journal*, 29 (6):422–427, 1959.

Van Den Oever, T. and Heiligers, J. On the Design of Transfers to Solar-Sail Displaced Orbits in the Earth-Moon System. In *7th International Conference on Astrodynamics Tools and Techniques*, Oberpfaffenhofen, 2018.

Wakker, K. *Fundamentals of Astrodynamics*. TU Delft Institutional Repository, Delft, 2015.

Wawrzyniak, G. and Howell, K. The solar sail lunar relay station: An application of solar sails in the Earth-Moon system. *International Astronautical Federation - 59th International Astronautical Congress 2008, IAC 2008*, 2008.

West, J. The Geostorm Warning Mission: Enhanced Opportunities Based on New Technology. *14th AAS/AIAA Space Flight Mechanics Conference*, 102, 2004.